DIPLOMARBEIT

Ultrafast Spectral Hole Burning Spectroscopy of Excitonic Transitions in Self-Assembled Quantum Dots

Ausgeführt am

Institut für Photonik
der Technischen Universität Wien

zum Zwecke

der Erlangung des akademischen Grades eines Diplomingenieurs

unter der Leitung von

Univ. Ass. Dr. Thomas Müller
und
O. Univ. Prof. Mag.rer.nat. Dr.rer.nat. Karl Unterrainer

durch

Thomas Moldaschl
Mayerhofgasse 3
A-1040 Wien

Wien, am 6. November 2006

Zusammenfassung

In dieser Diplomarbeit werden Messergebnisse ultraschneller zeitaufgelöster “Spektraler-Loch-Brenn” - Spektroskopie präsentiert, die an selbstorganisierten Indium-Arsenid / Gallium-Arsenid Quantenpunkten durchgeführt wurden. Quantenpunkte sind nulldimensionale Halbleiterstrukturen mit näherungsweise diskreten Zustandsdichten, weshalb sie oft auch als “künstliche Atome” tituliert werden.

Im Unterschied zu Atomen spielt bei Quantenpunkten die Wechselwirkung der elektronischen Zustände mit den Gitterschwingungen - genannt Phononen - des umgebenden Halbleiter Materials zusätzlich eine entscheidende Rolle. Diese sehr stark temperaturabhängige Erscheinung bewirkt eine Verbreiterung der Absorptionslinie, was auch als eine Verkürzung der Kohärenzzeit der elektronischen Zustände interpretiert und auch meßtechnisch nachgewiesen werden kann.

Da optische Übergänge in Quantenpunkten eine starke inhomogene Verbreiterung aufweisen, wurde die spektroskopische Technik des “Spektralen-Loch-Brennens” präferiert, um gezielt einen isolierten Teil der Punkte energetisch zu selektieren. Diese Technik erlaubt es daher auch Energiedifferenzen kleiner als die inhomogene Verbreiterung zu erfassen. Die Verbreiterung selbst rührt von unterschiedlich großen Quantenpunkt Abmessungen her, die auf die stochastische Selbstorganisation zurückzuführen sind.

Ein bislang eher theoretisches Konzept - das des Quantencomputers - beruht auf dem kohärenten nichtlinearen Effekt der Rabi Oszillation, die in stark angeregten Zwei-Niveau Systemen zu finden sind. Dieser fundamentale Effekt wurde im Rahmen dieser Arbeit in dem inhomogen verbreiterten Quantenpunkt-Ensemble nachgewiesen. Aufgrund der sogenannten Dephasierung kann die Kohärenz der Polarisation zur Anregung nicht beliebig lange aufrecht erhalten werden, weshalb die Oszillationen gedämpft sind. Dephasierung und Lebensdauer sind eng miteinander verknüpft, weshalb eine Erhöhung der Temperatur zu einem verstärkten Dämpfungsmaß führt, bis schließlich die Kohärenz vollständig verloren geht. Dieser Sachverhalt wurde durch das Erfassen der Oszillationen bei verschiedenen Temperaturen meßtechnisch belegt.

Unter gemäßigter Anregung - in dem von linearen Effekten dominierten Bereich - manifestierte sich die Temperaturabhängigkeit in den Meßergebnissen durch das Auftreten von Seitenbändern neben den schmalen Linien. Dieser Aspekt wurde bereits mehrfach in der Literatur beschrieben und in dieser Arbeit bestätigt. Weiters konnte gezeigt werden, daß bei Temperaturen ab etwa 90 K ein einfach exponentieller Abfall der Polarisation dem gesamten System Genüge leistet, und in sehr guter Übereinstimmung mit anderen Berichten in der Literatur steht.

Abstract

In this diploma thesis measurements, based on ultrafast time-resolved spectral hole burning spectroscopy, have been performed on an ensemble of self-assembled Indium-Arsenide / Gallium-Arsenide quantum dots. Quantum dots are zero-dimensional semiconductor structures with discrete density of states, which is why they are often referred to as "artificial atoms".

Unlike atoms, however, the interaction of electronic states with the propagating lattice displacement modes - the phonons - plays a major role, since the quantum dots are embedded in the crystal matrix. This effect strongly depends on the temperature and leads to a broadened absorption line, which corresponds to a shortened coherence time, that can be supported by measurements.

As the optical transitions in quantum dots show strong inhomogeneous broadening, spectral hole burning spectroscopy was the preferred measurement technique, since it is able to energetically select and resolve a fraction of the whole ensemble. Due to these properties it is able to observe energetic differences smaller than the inhomogeneous broadening. The broadening itself arises from size variations of the quantum dots due to the stochastic process of self-assembly.

A still rather theoretical concept, namely the concept of a quantum computer, basically relies on a coherent nonlinear effect, called the Rabi oscillation, that is found in strong optically excited two-level systems. This fundamental effect has been measured with the inhomogeneously broadened quantum dot sample in this thesis. Due to the so called dephasing the coherence between the polarization and the excitation cannot be maintained for an arbitrarily long time, which eventually leads to damping of the oscillations. Dephasing and lifetime are strongly linked together, resulting in a likewise increase of the damping with temperature, until coherence is totally lost and the oscillations disappear. This effect has been confirmed by experiments through the observation of the oscillations at different temperatures.

Under weak excitation - within the regime dominated by linear effects - the temperature dependence becomes manifest in the rise of phonon sidebands, right next to the purely electronic transition line. This effect has been known for a while in the literature, and has further been confirmed within this thesis. Furthermore it has been shown, that for temperatures higher than approximately 90 K, the phonon sidebands cannot be separated from the electronic transition line, leading to a simplified description of dephasing with a single exponential decay showing excellent agreement with other reports in literature.

Contents

Chapter 1

Quantum Dots - A Brief Introduction

At the beginning of the last century atomic physics progressed rapidly by the discoveries of quantization and spin, among others, through optical spectroscopy. The birth of the laser gave scientists the opportunity to control wavefunctions by the application of a coherent light field. And now, at the beginning of a new century another scientific frontier lies ahead: The emergence of the quantum computer - a concept that relies on the coherent control of states in a quantum mechanical regime. One of the most promising objects to incorporate these states, are quantum dots.

1.1 Designing Structures with Atom-like Behavior

Many milestones in fabrication technologies - such as the Molecular Beam Epitaxy, made it possible to design structures down to a size, where quantum effects dominate the overall behavior. The goal was to explicitly calculate the properties of a structure, thus "designing" it, and then fabricate it with an accuracy in the order of atomic dimensions. Prominent examples are quantum wells, quantum wires and quantum dots.

Fig. 1.1 shows the consequences of a successive increment of the degree of confinement. The black regions indicate a low-gap material, whereas white stands for high-gap material regions. This discontinuity in energy bands becomes manifest in the formation of potential wells of the conduction- and the valence band, thus, leading to quantization. If one considers the density of states for a bulk material, the continuity of the function $n(E)$ suggests a broad range of energies suitable for electronic transitions. Homogeneous linewidths in quantum dots are in the order of a few μeV [5], that is still significantly larger than for single atoms, but nevertheless a factor of 1000 smaller compared to a bulk material.

Quantum effects usually take place, once the dimensions go below atomic dimensions, that is around 1 nm, where the de Broglie wavelength of a particle exceeds its spatial dimension. In the case of a quantum dot, these effects extend to the dimensions of a dot, which is 10-100 nm. This, and the strong confinement, provides a total quantization of the system defined by the quantum dot. After excitation an electron is created, and a hole is left behind. Since free propagation is not possible, a new compound of an electron and

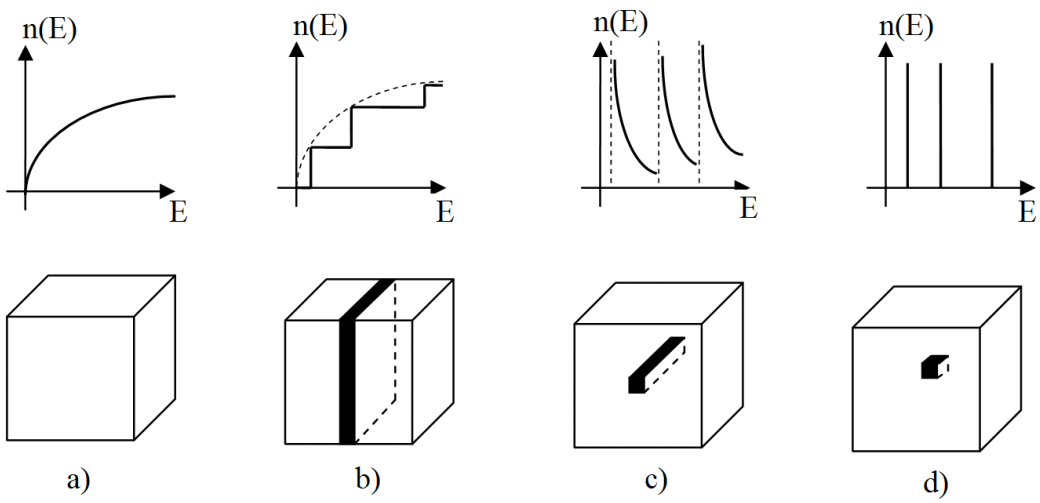

Figure 1.1: Density of States in a bulk semiconductor material a), in a quantum well structure b), in a quantum wire c) and in a quantum dot d)

a hole - called an exciton - is formed. This particle can be treated like a hydrogen atom, since it also consists of a positive- and negative charged particle encircling each other. The circular motion also constitutes spin. It even turns out, that the possible states of these excitons are very similar to the shell-like electron states in an atom. Pauli's exclusion principle, as well as Hund's rule are also applicable to the excitonic quantum dot system. That is why quantum dots are often referred to as "artificial atoms", or "designer atoms". As already indicated, the vast majority of experiments relies on optical spectroscopy, not only for atoms, but also for quantum dots. In order to perform spectroscopical measurements on isolated single atoms, atomic traps have to be installed, which constitutes a very high amount of experimental effort. These traps usually consist of two pairs of high energy lasers placed across from each other, providing a standing wave along their beams. Once their frequencies are detuned slightly, the positions and size of the field's maxima and minima can be designed to meet the setup dimensions. Those artificial potentials serve as atomic traps. Quantum Dots, however, are confined in a solid lattice, which makes them a lot easier to handle. Another advantage of quantum dots over single atoms is the ability to apply electrical contacts, in order to excite the system electrically. Since their behavior is atom-like and are easy to handle, they are very promising objects to replace atoms and all their implementations for e.g. quantum computing. Fig. 1.2 shows the photoluminescence (PL) spectrum of a single self assembled InAs-GaAs quantum dot, providing sharp atom-like transitions from the excited s- and p-states to the ground state. As indicated, there even exists an association of states with shells (s, p) that can be distinctly separated in the energy domain. The reason for the presence of the so called wetting layer in self-assembled quantum dot structures will be discussed later, but only concerning the PL spectrum, it shows a comparably broad line, unlike the dot transitions, since this layer constitutes a quantum well structure with a lower degree of confinement.

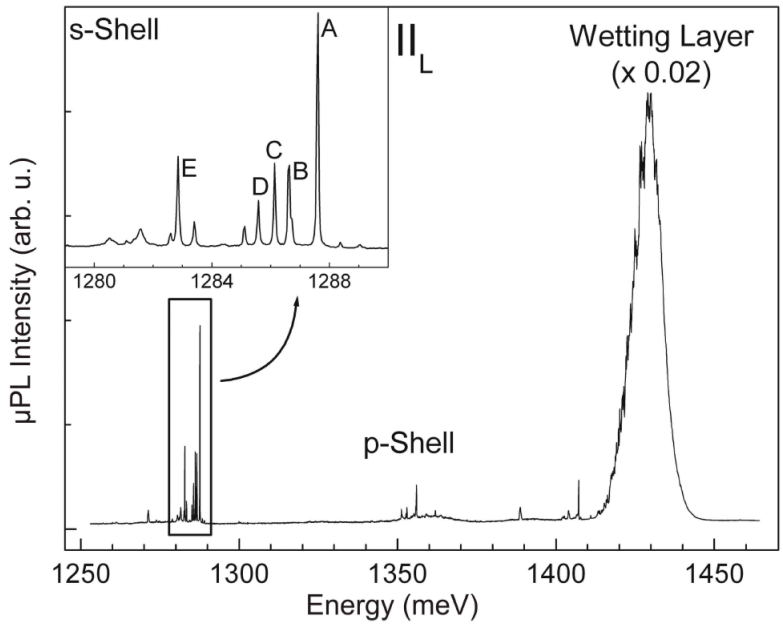

Figure 1.2: Photoluminescence measurements in a single Quantum Dot showing atom-like transition spectra [4].

1.2 Manipulation with Light - or the Idea of a Quantum Computer

Still in the dawn of existence, thus a rather theoretical concept, quantum computation is gaining more and more scientific, as well as public interest. Since Moore's law is not applicable for an infinite time, there have to be concepts of technological successors to the binary computer systems used at present. Conventional silicon based CMOS technology used for almost all semiconductor based components in a computer system is already stretching the boundaries of Moore's law by approaching the quantum limit. Structure sizes down to 65 nm are almost in the same order as the dimensions of quantum dots are.

Classical computers based on semiconductors are also bound by quantum mechanical rules, however, they depend on aggregates of large numbers of quantized entities. Hence, computation speeds are limited compared to transition speeds of single-, or few-particle systems, such as atoms or Quantum Dots. The key element to build a quantum computer is to gain control over these transitions by using optical excitations for starters and electrical controls in the near future.

There is one outstanding optical control mechanism suited for that - the Rabi Oscillation. As it will be shown later, the occurance of this non linear phenomenon depends on the strength of the interacting lightfield, as well as the dipole moment. The latter one is 50 - 100 times larger in quantum dots, than in atoms, which makes quantum dots a perfect candidate for the use in a quantum computer based on Rabi flopping [1]. Fig. 1.3 shows a damped sinusoidal oscillation as it appears in a real quantum dot system.

Analogously to the bit for computers based on binary operations, the qubit is introduced as the basic unit in quantum information processing and consists of two distinctive

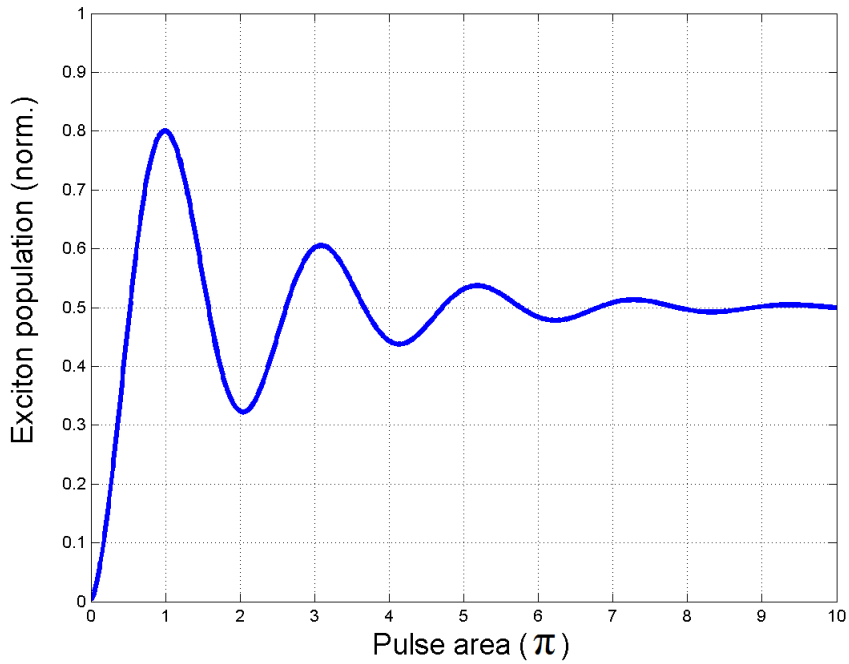

Figure 1.3: Qualitative picture of damped Rabi Oscillations. An inversion of the population occurs every π^{th} pulse area increment.

orthogonal excitonic states $|0\rangle$ and $|1\rangle$. What the signal of fig. 1.3 also indicates, is the major difference between the binary case scenario: The qubit can take on any linear combination of the two states, thus, containing vastly more information than a classical bit is capable of. This also leads to the possibility of massively parallel processing. Let

$$\Theta_R = \int_{-\infty}^{\infty} \Omega_R(t)\, dt, \tag{1.1}$$

denote the time integral of the Rabi frequency $\Omega_R(t) = \frac{d_{01}E}{\hbar}$, with d_{01} being the dipole moment and E the amplitude of the electrical field component. Since Θ_R is called the pulse area - Ω_R is directly proportional to the strength of the electrical field of the exciting coherent pulse, and the dipole moment is time independent, the quantum mechanical state describing this oscillation, without damping, would be [1]

$$|\Psi(t)\rangle = \sin(\Theta_R/2)|0\rangle + \cos(\Theta_R/2)|1\rangle. \tag{1.2}$$

Since the measurement data is taken at a certain photon energy - let's say at the energy associated with state $|1\rangle$, the sinusoidal oscillation behavior can be observed directly.

In order to process information there have to be some basic functional elements, the gates - similar to the binary logic gates. These gates can involve the manipulation of an arbitrary number of qubits. The problem that arises, as we will see later, is to find a suitable system providing 2^N states in order to establish an N qubit gate. However, even a set consisting of a single qubit rotation gate and a non trivial 2 qubit gate are sufficient

to develop quantum algorithms based on this set. Furthermore, an N qubit gate can be decomposed in terms of two qubit gates. At present there only exist a few algorithms suitable for being implemented using such a set of processing gates. A very prominent example is Shor's algorithm for quantum fourier transform, which is best known for its application in the prime factorization of large numbers, thus for cryptography [2]. Another example would be Grover's search algorithm [3].

Single Qubit Gates based on Quantum Dots

A single qubit, defined by the ground- and excited state of an exciton, can be manipulated with suitable pulses by Rabi oscillations. If a π-pulse is applied, the qubit would be inverted. The inverter gate would define the single qubit gate in the set. These pulses, produced by a pulsed laser system, are usually in the picosecond range. Hence, the inversion itself is only limited by the temporal dimension of the exciting π pulse, or the strength of the electrical field - which defines the pulse area.

Two-Qubit Gates based on Quantum Dots

The excitonic energy system of a quantum dot is a very good example for a two-qubit gate, called the CNOT gate. Fig. 1.4 shows the energy structure of this system. The $|00\rangle$ state represents the crystal ground state without any excitation, whereas the $|01\rangle$ and the $|10\rangle$ states represent excitonic states excited with differently polarized light. The compound consisting of two differently excited excitons is called a biexciton and is represented by the $|11\rangle$ state. The path that leads to the biexciton - left or right - is predetermined by the polarization of the excitation, σ_+ and σ_-, respectively. It should be noted, that the biexciton's energy is less than the sum of the energies of two separate excitons, thus, incorporating a binding energy due to Coulomb interactions within the strong spatial confinement of the dot. In other words, the creation (excitation) of an excitonic state with certain energy in a quantum dot depends if there already exists an excitonic state or not. In one case a lowered binding energy is needed in order to create $|11\rangle$ out of $|10\rangle$ or $|01\rangle$, and the other case describes the creation of $|10\rangle$ or $|01\rangle$ out of $|00\rangle$ with a higher energy. This very important fact gives rise to a path selection scenario, that is needed to incorporate a CNOT gate.

The function of a CNOT gate is to control the inverters operation. Once the control qubit is turned on, the inversion of the second qubit shall be performed, and it should remain unchanged, if the control qubit is turned off. This leaves a functional description of the CNOT gate as

$$|00\rangle \longrightarrow |00\rangle, \quad |01\rangle \longrightarrow |01\rangle, \quad |10\rangle \longrightarrow |11\rangle, \quad |11\rangle \longrightarrow |10\rangle. \tag{1.3}$$

In order to enable this kind of function, a π rotation must be performed between states $|10\rangle$ and $|11\rangle$, thus, toggling between those states by a proper π Rabi oscillation, enabled by an excitation designed to just affect these two states constituting a two level system, but without inducing other transitions such as $|00\rangle$ and $|01\rangle$. Once this function is established, an inversion is only performed, if the control qubit is active - that is the function of the CNOT gate.

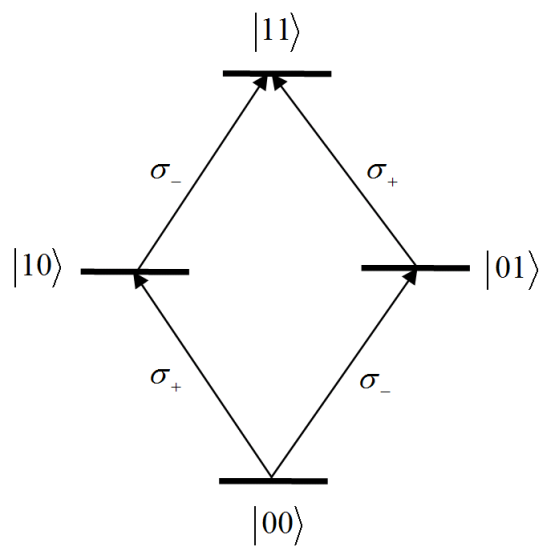

Figure 1.4: Two-Qubit CNOT Gate realized with the excitonic energy structure of a quantum dot

The biggest obstacles to overcome, in order to provide a stable and sufficiently precise quantum information processing system, are to counter dephasing. This effect describes the loss of phase coherence, that leads to the damping effects shown in Fig. 1.3. Since the oscillations do not endure for an arbitrarily long time, the functionality of an N-qubit gate would be coherence bound in time. One possible solution to bypass this problem is to introduce quantum error correcting mechanisms. There have been several attempts to manipulate excitonic qubits in quantum dots [6]. It should also be noted that an N-qubit gate would require a system of 2^N orthogonal states, that must, depending on the functionality, be optically accessed for almost all of the possible branches individually. This represents a major challenge, since it goes far beyond the "design" of atoms - like for quantum dots. Very promising candidates for these systems are quantum dot molecules [7].

Chapter 2

Theoretical Background

2.1 Fabrication and Structural Properties of Quantum Dots

The path from a bulk semiconductor material to a quantum dot is determined by successive confinement - first in one, then in two, and eventually in all three spatial dimensions. There are many ways to manufacture quantum dots, since there are many different potential materials of interest. The most commonly used compounds are III - IV Semiconductors such as GaAs and InAs. But there are also II - VI compounds like CdS, CdSe and CdTe. Early studies of quantum dot structures have even been conducted with chemically synthesized CuCl dots embedded in a NaCl Matrix.

2.1.1 Manufacturing Processes of Quantum Dots

As depicted in equation (2.1) the three dimensional confinement of the low energy gap material in the high gap material leads to a 3 - dimensional finite quantum well [4]. In each direction the confinement yields a solution to the Schrödinger equation - using an infinite well approximation, of

$$E_l = \frac{(l+1)^2 \pi^2 \hbar^2}{2m^* d^2} \tag{2.1}$$

where l is an integer ≥ 0, showing the quantization nature of the confined system, m^* denotes the effective mass of the particle (electron or hole) and $2d$ is the width of the dot. The energy difference between two states l and $l+1$ is minimum for $l = 0$, since the energy increases quadratic with l. This minimum difference shall be in the same order as, or bigger than three times the thermal energy kT, in order to distinguish all the states even at room temperature.

Hence,

$$\Delta E_{min} = E_1 - E_0 = \frac{3\pi^2\hbar^2}{2m^*d^2} \geq 3kT \tag{2.2}$$

leaves a design criteria for the dots. Since m^* is fixed for a certain material, one can obtain d from this equation. The effective mass for electrons in InAs is about $0.023 \cdot m_0$, where m_0=$9.11 \cdot 10^{-31}$ kg, is the mass of a free electron. Thus, using a thermal energy at room temperature of 25 meV, the upper bound of d - considering electrons - for InAs quantum dots can be obtained as:

$$d = 25.6 \text{ nm} \tag{2.3}$$

Self-Assembly

One Method to grow quantum dots is self-assembly. This technique was used to grow the sample that was used in this thesis. It simply uses the fact, that for instance the two binary compounds InAs and GaAs have different lattice constants. First one starts with a GaAs substrate, then growing a thin so called "wetting layer" of InAs via molecular beam epitaxy. Since there is a lattice mismatch, the InAs layer is strained, thus leading to new surface energy equilibrium states, becoming manifest in the formation of well separated island-like structures - the quantum dots. Unfortunately this strain is not isotropic, leading to elliptically-shaped dots instead of a circular shape. As we will see later, this has an impact on the optical properties. The reason why these dots are usually embedded in a capping layer, is because the edge effects of the dots would influence the characteristics, thus leading to transition shifts. Fig. 2.1 shows the successive process of self-assembly. An

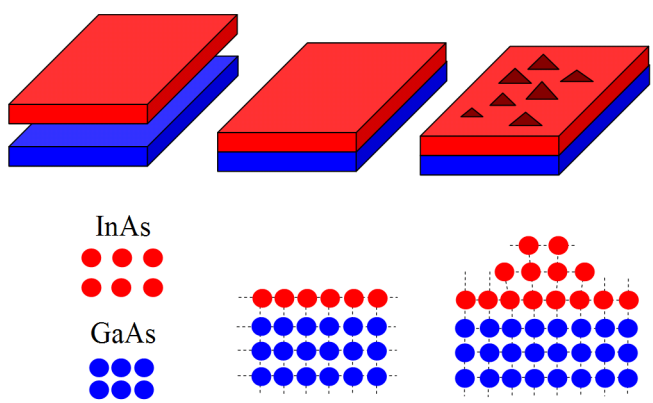

Figure 2.1: The self-assembly of quantum dots using the III-V binary compounds InAs and GaAs, respectively

atomic force microscope (AFM) image of self-assembled InAs quantum dots is revealed in fig. 2.2 a). To enhance visibility in a two-dimensional picture, lighting and the resulting shading is added to the original three-dimensional data. This image also reveals an elliptical shape, unlike the expected circular shape. According to this picture the [1-10] direction seems to be stretched, or, equivalently, the [110] direction appears compressed. Part b) shows a one-dimensional Fourier transform of this data along the [110] direction,

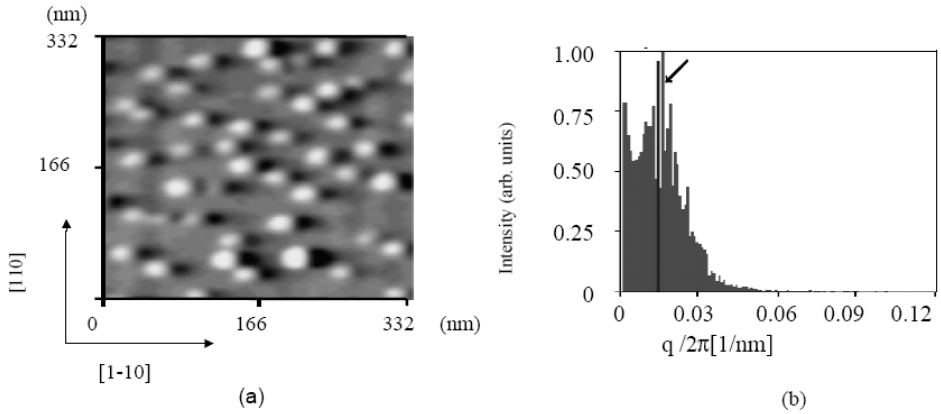

Figure 2.2: AFM image of self-assembled InAs quantum dots a) and a one-dimensional Fourier transform of the data in a) along the [110] direction shown in b)[8]

showing a comparably broad spectrum of $1/d$ due to inhomogeneous broadening. This spectrum can be interpreted as a measure for the energetic inhomogeneous broadening as well.

Photolithography

A more intuitive method, using only semiconductor mass production equipment, is photolithography. Through the application of this standard tool, size and position of the dots can easily be determined. There are two major drawbacks though. The first one arises from the spatial limitations of the lithographic method, that can only produce dot sizes down to 30 nm. The second drawback results from the etching process, leaving uneven surfaces resulting in a poor radiative efficiency.

Chemical Methods

In an early stage of quantum dot investigation chemically produced nanocrystals with semiconductor properties have been used. Once these crystals are embedded in a high gap matrix, they are called colloidal quantum dots. An example of such a combination is CuCl crystals in a NaCl surrounding. First CuCl must be dissolved in a suitable solvent, then the temperature is increased until supersaturation is achieved, thus, leading to nucleation. CuCl quantum dots can be classified as weakly confined, since the dot radius is bigger than their respective exciton Bohr radius, i.e. electrons and holes are not quantized individually, as in a strong confinement system where the exciton bohr radius is bigger than the dot size, but where the translational motion of the exciton is quantized [9].

2.2 Electronic Properties

Comparing a zero dimensional quantum dot to its three dimensional bulk material counterpart one can immediately see, that the wave functions, describing carriers in a quantum

dot, have to be strongly localized. Using Heisenberg's uncertainty principle

$$\Delta p \Delta x \geq \frac{\hbar}{2} \tag{2.4}$$

where Δp is the uncertainty in momentum, Δx the one for the position, we obtain an overwhelming uncertainty of the momentum of the carrier. That is why in a quantum dot there is no dispersion relation for carriers (energy vs. momentum), unlike a bulk material. Which makes sense considering the three dimensional trap of the carrier that prohibits free propagation. In the case of a bulk semiconductor material Bloch's theorem states, that a particle trapped in a periodic potential features a periodic wavefunction as well - that is infinitely long. This however initially enables the momentum of a carrier to be determined with an arbitrarily large accuracy, thus leading to a possible dispersion relation and conductivity. Carriers can be electrons, holes and electron - hole pairs, called excitons.

2.2.1 Excitonic States in a Quantum Dot

In order to see the fundamental properties of the electronic states in a quantum dot system we are making the following assumptions. As stated earlier, the confinement of a carrier in a dot like structure varies from weak to strong, depending on the material. Taking the very strong vertical confinement into account - since the dot height for self - assembled quantum dots is a lot smaller than its lateral dimension (5 nm compared to 30 nm), the carrier finds itself within a horizontal two dimensional harmonic oscillator, vertically confined by an infinite potential well.

The Hamiltonian of such a system is the sum of the Hamiltonian of a two dimensional harmonic oscillator

$$H_{xy} = \frac{1}{2m^*_{e/h}}(p_x^2 + p_y^2) + \frac{1}{2}m^*_{e/h}\omega^2_{e/h}(x^2 + y^2) \tag{2.5}$$

where $m^*_{e/h}$ denotes the mass of an electron/hole, $\omega_{e/h}$ is the harmonic oscillator frequency of an electron/hole, x and y are the lateral coordinates and p_x and p_y are the respective lateral components of the momentum and the Hamiltonian of an infinite potential well located in between z = -d and z = d

$$H_z(z) = \begin{cases} 0, & |z| \leq \text{d} \\ \infty & \text{elsewhere} \end{cases} \tag{2.6}$$

(2.6)is the classical quantum mechanical problem describing a single particle fully trapped in a one dimensional box leading to (2.1), whereas (2.5) describes the parabolic potential energy distribution from the harmonic oscillator model. Since we are only interested in the stationary solution to this problem, the Schrödinger equation breaks down to the eigenvalue problem

$$H_{xyz}|\Psi\rangle = E_{l,m,n}|\Psi\rangle \tag{2.7}$$

given

$$H_{xyz} = H_{xy} + H_z \tag{2.8}$$

leading to the eigenvalues [10]

$$E_{l,m,n} = \frac{(l+1)^2\pi^2\hbar^2}{2m^*_{e/h}d^2} + (m+n+1)\hbar\omega_{e/h} \tag{2.9}$$

where the first summand is just (2.1), thus, l is a positive integer including 0, as are m and n, respectively. Again, the effective mass is $m^*_{e/h}$ and $\omega_{e/h}$ is the oscillation frequency of an electron/hole. Since d is fairly small - $2d$ are in the order of 50 nm for self assembled InAs - GaAs quantum dots, the expected level spacing is pretty big. It even turns out, that excited states are unbound, thus not contributing to the excitonic system and treating the z - direction part in the energy equation as a constant summand with $l = 0$. What we can immediately see is the degree of degeneracy of the energetic eigenvalues. Since every $m + n = const.$ leads to the same energy we conclude that the energies are $(m+n+1)$ - fold degenerate. Also we see the energy itself being directly proportional to $(m+n+1)$ - up to a constant. It also turns out, that the angular momentum L_z in the z - direction, resulting from the harmonic oscillator problem in the x, y - plane, is in the form of

$$L_z = \hbar k \tag{2.10}$$

where k is a positive or negative integer or zero and is restricted in terms of $m - n$. Including spin eq. (2.9) and eq. (2.10) leave a total degree of degeneracy of $2(m+n+1)$ [10]. Fig. 2.3 shows the consequence of the degeneracy. It should be noted that Pauli's exclusion principle, as well as Hund's rule is in accordance with these results. Since these findings look very similar to the shell structure of an atom, successive levels are also associated with the orbitals s, p, d, ... Hence optical transitions between states are restricted in terms of energy and angular momentum. Using a dipole approximation of an exciton, a photon can only be created if the total angular momentum between two states differs only in ± 1. Using $\pm\frac{1}{2}$ as the spin for electrons and $\pm\frac{3}{2}$ for holes the total angular momentum for the states in fig. 2.3 becomes $L_{tot,e} = L_z \pm \frac{1}{2}$ and $L_{tot,h} = L_z \pm \frac{3}{2}$, respectively.

Taking into account the ± 1 difference in angular momentum fig. 2.3 shows the possible optical transitions s-s, p-p, ... as well as s-d and vice versa.

2.2.2 Few - Body Interactions

The preceding section dealt with a system consisting only of a harmonic potential in the x, y - plane without considering interactions between the particles. As one can imagine especially the attractive or repulsive coulomb interaction between electrons and holes will influence the overall behavior of the dot as well as the harmonic potential. This may even split originally degenerate energies in a real dot system.

The classification of the confinement regime will also influence the interaction. The bigger the exciton Bohr radius compared to the lateral dot size, the more crowded are electrons and holes forming the exciton, thus leading to stronger Coulomb interactions, whereas bigger dot dimensions lead to less interactions. The Coulomb potential, given two charged particles i and j with charge q_i and q_j, respectively, is given by

$$V_{i-j} = \frac{q_i q_j}{4\pi\epsilon_0\epsilon_r r}, \tag{2.11}$$

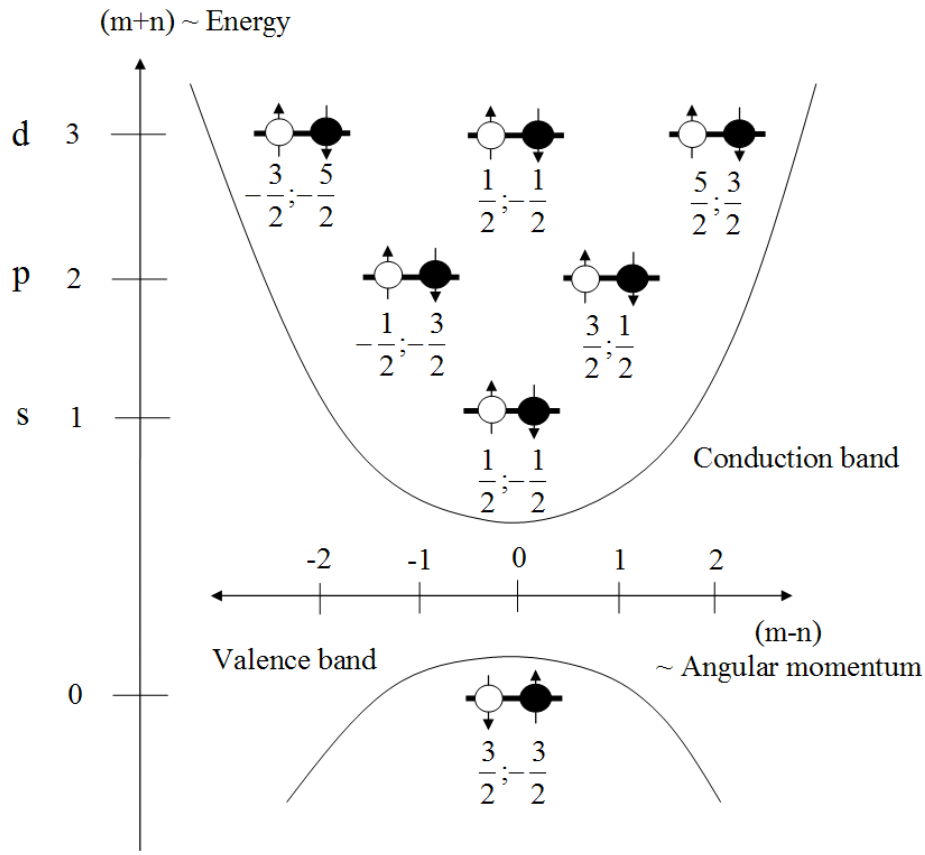

Figure 2.3: Allowed orbital states in a two dimensional harmonic oscillator.

where ϵ_0 is the dielectric constant in vacuum, and ϵ_r denotes the dielectric constant of the dot material.

Taking the Coulomb potential into account, by using fig.2.4 a), the energy of an exciton in the ground state is rewritten as [11]

$$E_X = \hbar(\omega_e + \omega_h) + \langle 1,0;1,0|V_{e-h}|1,0;1,0\rangle \tag{2.12}$$

In $|1,0;1,0\rangle$, the first pair denotes the number of electrons in the s, p state, the second pair the number of holes. It should be noted that a harmonic potential in the lateral dimensions is still the only model assumption, therefore neglecting the potential well in z-direction. Since InAs has a very narrow energy gap, the conduction and the valence band cannot be treated separately, since they interact with each other [11]. This effect, as well as the interference between light- and heavy hole bands is ignored in this discussion.

As one can imagine, the attraction between two oppositely charged particles and the repulsion between equally charged particles leads to a decreased and an increased energy, respectively, compared to the harmonic oscillator model. However, defining an excitonic binding energy is a theoretical task, since it is a matter of definition if this binding effect is already incorporated to the quantum dot potential or not. Furthermore, the binding energy of a single exciton cannot be measured and has therefore no clear physical meaning.

Looking at a quantum dot containing two excitons, a biexciton, the situation is quite

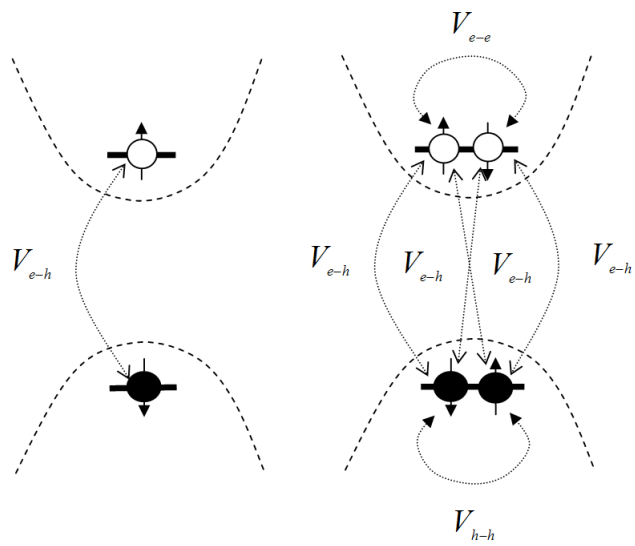

Figure 2.4: Coulomb interactions of electrons and holes in a) an exciton and b) in a biexciton

different. Fig.2.4 b) shows all possible interactions between 2 electrons and 2 holes forming the biexciton. The energy of the four - particle system in the ground state, E_{2X}, can be written as [4]

$$E_{2X} = 2E_X + \langle 1,0;1,0|V_{e-e}|1,0;1,0\rangle + \langle 1,0;1,0|V_{e-h}|1,0;1,0\rangle + \\ + \langle 1,0;1,0|V_{h-h}|1,0;1,0\rangle + \langle 1,0;1,0|V_{e-h}|1,0;1,0\rangle \tag{2.13}$$

In a perfectly symmetric dot system all 4 interaction contributions cancel each other, thus leaving the biexciton binding energy as twice the exciton energy. If this is the case, it means that a biexciton is not able to recombine directly. Each of the two excitons recombines separately, with each creating a photon. So every photon has the energy of an exciton, meaning that the ground state is degenerate. This is in accordance with the harmonic oscillator model.

In a real quantum dot, symmetry cannot be guaranteed, even within the same sample [8]. Other reasons for the deviation of the biexciton binding energy can be due to different confining potentials of electrons and holes, or simply because of different effective masses. Once these changes occur, the cancellation of the four interaction terms is lost, leaving a biexciton binding energy different from the double exciton energy. But there are no a priori estimates for the difference, not even for the sign of it, upon fabrication.

Since the states appear non - degenerate due to the shift, there can be only one excited state with this energy. If one photon excites this state resonantly, a second one with the same energy would not be absorbed any more until the exciton vanishes due to recombination. During the time the exciton exists the whole dot would appear transparent for this certain energy.

2.3 Optical Properties - Interaction with Light

To excite a state in a perfectly symmetric quantum dot, circularly polarized light is used. This is rather intuitive considering a very classical interpretation of the spin as a rotational motion of an electrically charged particle. A circularly polarized photon will either excite a dot or not, depending on whether the electron is spinning up or down [5]. In a real quantum dot, due to the asymmetric size, actual states are a superposition of two opposite spin excited states.

As a consequence a different photon polarization is necessary to excite this state. Since the superposition of a clockwise circularly polarized photon, having a certain energy, and a counterclockwise circularly polarized photon, having the same energy, results in a linearly polarized photon, one needs a linearly polarized photon source, instead of a circular one, to create an exciton. Fig. 2.5 shows the possible paths to create excitons and biexcitons. The green paths indicate the allowed transitions while the red ones

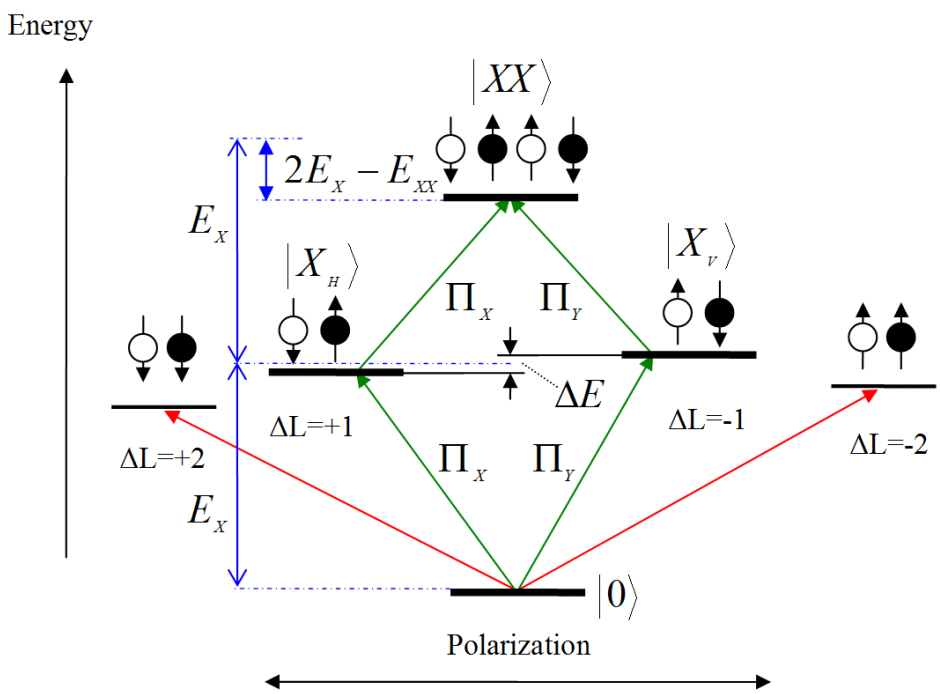

Figure 2.5: Possible optical transitions for creating an exciton (X) and a biexciton (XX)

are not accessible through optical excitation, since the angular momentum difference, as indicated, $\Delta L = \pm 2$. The only difference between the path Π_X and Π_Y is the direction of the linearly polarized photon, namely, they have to be orthogonal (defining the X-direction as horizontal and the Y-direction as vertical, leading to excitonic states $|X\rangle$ with subscripts H and V, respectively). It should be noted, that the excitation energies for the two possible polarization paths are not the same. The reason for this splitting comes mainly from the non - circular shape of the dots, namely from elongation in [1-10] direction - as seen in fig. 2.2.

2.4 Phonons in Quantum Dots

The loss of phase coherence of an excitonic state in a quantum dot is the main obstacle to overcome, if one wants to build a quantum computer based on quantum dots. This still rather theoretical construct basically relies on coherent effects such as Rabi oscillations. Contributions to dephasing are mainly due to scattering processes of excitons with phonons, eventually leading to relaxation, that can also be interpreted as dephasing due to population decay. Among the physical mechanisms responsible for the dephasing, the interaction of excitons with phonons in quantum dots is a topic intensively discussed in the literature and still under debate [12].

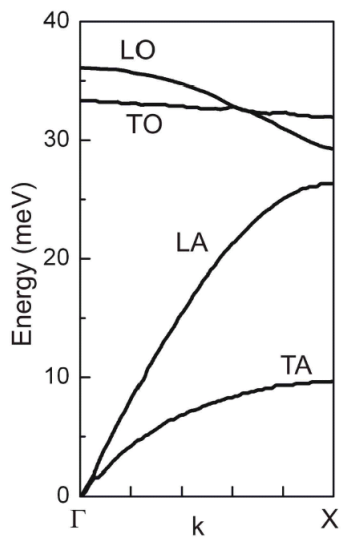

Figure 2.6: Dispersion relation of the continuous spectra of phonon eigenstates in GaAs, responsible for the range of interaction with excitons in order to obey the conservation laws of momentum and energy.

2.4.1 Relaxation

Carrier relaxation results from the interaction of a carrier with its surrounding. It involves a series of inelastic scattering events accompanied by a permanent exchange of energy and momentum, eventually leading to a new stationary state. Relaxation due to phonon scattering must, of course, obey the conservation laws of energy and momentum, thus limiting the possible contributions of phonons involved in the process. Since the density of states in a quantum dot is discrete, there are further limitations on the phonons. These aspects lead to a problem often referred to as the "phonon bottleneck", which infers the interaction of a continuous spectrum of phonons , as indicated in fig. 2.6, with the discrete spectrum of excitonic states [13]. So there have been several ways for explanations of this problem - e.g. multiphonon processes [14] or polarons [15].

Multiphonon processes are several inelastic and uncorrelated phonon scattering incidents eventually leading to a total relaxation. If the scattering event of the exciton with a phonon having mode q has probability p_q, then the scattering of N phonons with the

exciton has probability p_q^N which becomes less and less probable, the more phonons are involved. Thus the most likely processes only involve a few phonons, but, in order to maintain the conservation laws, they consist of a mixture of acoustic and optic phonons.

A polaron is the combination of an electron and a phonon, in a way, that they coherently exchange energies, and can be seen as a single particle with its own wavefunction. If the electron loses its energy non reversible by creating an additional phonon, the relaxation process is complete.

2.4.2 Dephasing

Dephasing describes the gradual loss of the phase relation between the polarization of a two-level system and the coherent light field exciting it.

$$\frac{1}{T_2} = \frac{1}{2T_1} + \frac{1}{T_2^*} \tag{2.14}$$

is derived from the optical Bloch equations, where T_1 is the population relaxation time from the upper level to the lower level, T_2 characterizes the decay of phase coherence between the two levels, whereas T_2^* is accounted for pure dephasing - a mechanism solely affecting the phase of the polarization. Hence, dephasing can have many contributions. Except for the phonon induced relaxation case, the dephasing through phonons can be attributed to pure dephasing. This is also rather intuitive, considering the scattering process and its effect on the wave function of the excitonic state, thus leading to a different phase distribution of the polarization.

There have been several attempts to quantify and predict measurement results of the effects of phonons on excitons [16] [17]. One possible approach to this problem shall be depicted. It is based on an extension of the Huang - Rhys theory of localized electron-phonon interactions, to the excitonic system [16].

The inset of fig. 2.7 shows the consequences of a propagating phonon in the crystal lattice. The vibrational motion of the lattice induced by the propagation leads to a lattice displacement, thus a change of the potential surrounding the exciton. This, of course, changes the Hamiltonian of the whole system as well. It should be noted, that the potential is, again, parabolic in the lateral directions, showing the harmonic oscillator assumptions. The major difference of this approach compared to ones carried out before, is to modify the Hamiltonian in a way that the exciton - phonon interaction is no longer considered as a perturbation of the system, but taking the new eigenstates of the coupled system of discrete excitonic states and the continuum of phonon states into account. As a result the coupling constant $g(q)$ is shown in fig. 2.7 as a function of the phonon energy $\hbar\omega_q$, where q indicates the phonon mode. The excitonic state was chosen to have a quasi-two-dimensional wavefunction with a Gaussian distribution for the center of mass motion, described by the localization parameter ξ.

Another result from fig. 2.7 is a strong dependence of the coupling constant on the energy of the phonon, or, equivalently, on its wave vector. Only phonons within a certain energy / wave vector - range are able to interact with the exciton, described by its characteristic localization length ξ. It turns out, that the coupling is most efficient, i.e. $g(q)$ is maximum, if the wave vector of the phonon q is in the order of $\frac{1}{\xi}$. All other phonons do not

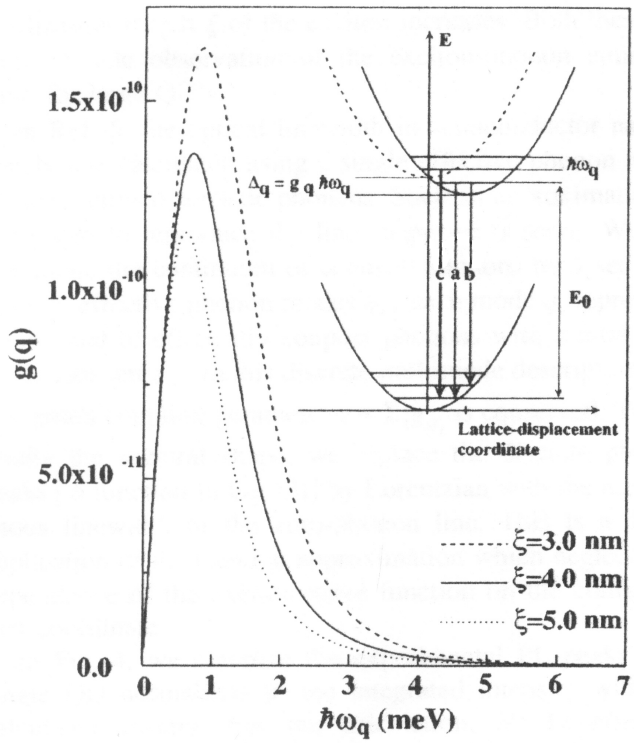

Figure 2.7: Coupling constant g of phonons having energies $\hbar\omega_q$ with the excitonic system; the inset shows a phonon propagation induced lattice displacement [16].

seem to contribute to dephasing. As one can imagine, the number of phonons available for the lattice system strongly depends on the temperature - the higher the temperature, the more phonons available, thus, higher dephasing rates.

So the scattering processes between excitons and phonons lead to fast dephasing, compared to the homogenous linewidth caused by the relatively long lifetime of the excitonic state. While the lifetime of excitons is in the order of nanoseconds [18], the phonon induced dephasing rate is - depending on the temperature - in the order of picoseconds [19]. Using the Fourier transform properties, the fast initial dephasing corresponds to a comparably broad spectrum of the underlying dephasing process, whereas the lifetime of the exciton itself provides a very small spectral linewidth. Since the lifetime can be modelled as an exponential decay, the corresponding shape of the exciton line is Lorentzian and is also called the zero phonon line (ZPL). Once the phonon interactions are taken into account, a broad phonon pedestal appears that is somewhat temperature dependent. Fig. 2.8 shows the temporal loss of phase coherence using four-wave mixing techniques [12]. The initial fast decay accounts for the exciton - phonon interaction, while the slow exponential decay shows the linewidth due to lifetime. Phonon pedestals are shown in the next chapters as the results of measurements.

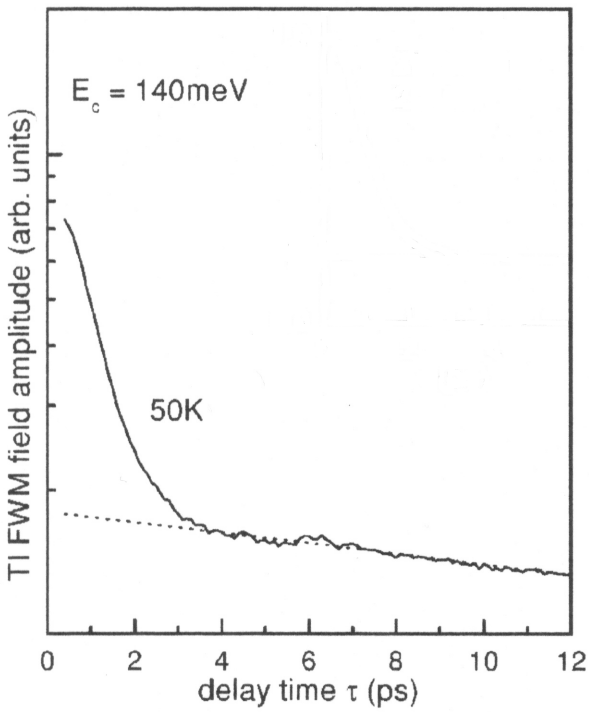

Figure 2.8: Time-integrated FWM field amplitude at 50 K [12].

2.5 Coherent Control of Quantum Dots - Rabi Oscillations

A phenomenon, called Rabi oscillations, occurs in strong coherently optical excited two-level systems. This effect has been verified through measurements several times for various structures, like atoms [20], and also lately - as well as in this thesis, for quantum dot structures. Optical Rabi Oscillations are a fundamental example of coherent nonlinear light-matter interactions building the foundation for quantum computing. Once a two-level system is exposed to a high energy light field, a periodic population inversion between the two levels occurs as long as the field is present. The frequency of this oscillation - the Rabi frequency, is proportional to the dipole moment and the light field. As a consequence of this effect, a two-level system can not be used as a laser, since the necessary population inversion occurs and vanishes periodically over time. Although it is always considered for a basic laser understanding, there has to be a three, or more-level system to induce lasing.

2.5.1 Rabi's Formula

In this derivation damping is ignored. In order to include it, one needs to solve the nonlinear optical Bloch equations. This only holds true as long as phonons are not included, because, as we have seen earlier, phonon dephasing processes lead to an overall non-Lorentzian line shape, thus the underlying dephasing processes are no longer Marko-

vian and making the Bloch equations inadequate. Perturbation theory does not include damping, though it provides the necessary insight for the periodic population inversion which is why it has been used in this thesis.

First we consider the two-level system depicted in Fig. 2.9 to determine the stationary eigenstates without perturbation. Since we are only interested in the stationary states, in

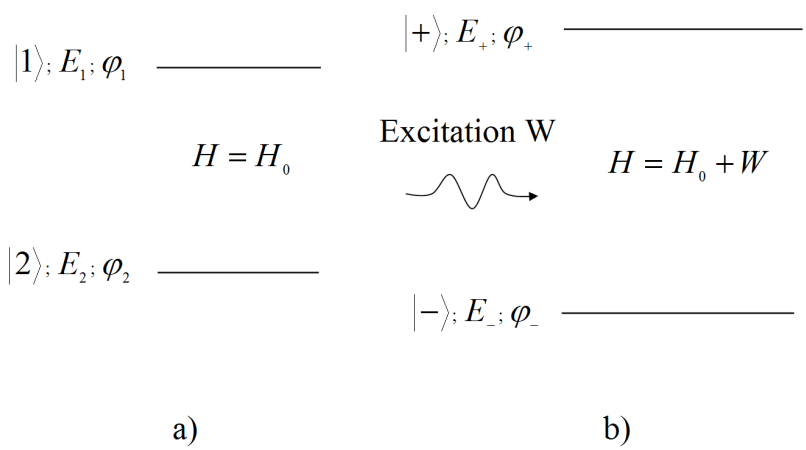

Figure 2.9: The two-level system having stationary states $|1\rangle$ and $|2\rangle$ with their respective energies E_1 and E_2 before excitation a) and having states $|+\rangle$ and $|-\rangle$, corresponding to E_+ and E_-, respectively, after excitation W b).

order to perform perturbation calculation, the Schrödinger equation breaks down to the eigenvalue problem, first for the original system without excitation

$$\begin{aligned} H_0|\varphi_1\rangle &= E_1|\varphi_1\rangle \\ H_0|\varphi_2\rangle &= E_2|\varphi_2\rangle, \end{aligned} \tag{2.15}$$

and second for the excited system

$$\begin{aligned} H|\varphi_+\rangle &= E_+|\varphi_+\rangle \\ H|\varphi_-\rangle &= E_-|\varphi_-\rangle. \end{aligned} \tag{2.16}$$

H_0 denotes the Hamiltonian for the unperturbed system, and $H = H_0 + W$ is the Hamiltonian of the system in the presence of optical perturbation. The basis, formed by φ_1 and φ_2, is assumed to be orthonormal. Furthermore,

$$(W) = \begin{pmatrix} W_{11} & W_{12} \\ W_{21} & W_{22} \end{pmatrix} \tag{2.17}$$

is the perturbing Hamiltonian, where W_{11} and W_{22} are real valued, thus making $W_{12} = W_{21}^*$, and the W_{ij} will get a meaning at the end of this discussion, simply to save some space.

In the $|\varphi_1\rangle, |\varphi_2\rangle$ basis, the matrix representing H is written:

$$(H) = \begin{pmatrix} E_1 + W_{11} & W_{12} \\ W_{21} & E_2 + W_{22} \end{pmatrix} \tag{2.18}$$

After diagonalization, the new eigenvalues of the perturbed system become

$$E_+ = \frac{1}{2}(E_1 + W_{11} + E_2 + W_{22}) + \frac{1}{2}\sqrt{(E_1 + W_{11} - E_2 - W_{22})^2 + 4|W_{12}|^2}$$
$$E_- = \frac{1}{2}(E_1 + W_{11} + E_2 + W_{22}) - \frac{1}{2}\sqrt{(E_1 + W_{11} - E_2 - W_{22})^2 + 4|W_{12}|^2}, \tag{2.19}$$

and the new eigenstates expressed in the original basis are [10]

$$|\varphi_+\rangle = \cos\frac{\theta}{2}e^{-i\varphi/2}|\varphi_1\rangle + \sin\frac{\theta}{2}e^{i\varphi/2}|\varphi_2\rangle \tag{2.20}$$
$$|\varphi_-\rangle = -\sin\frac{\theta}{2}e^{-i\varphi/2}|\varphi_1\rangle + \cos\frac{\theta}{2}e^{i\varphi/2}|\varphi_2\rangle, \tag{2.21}$$

where Θ and φ are defined by

$$\tan\theta = \frac{2|W_{12}|}{E_1 + W_{11} - E_2 - W_{22}} \quad \text{with} \quad 0 \leq \theta < \pi \tag{2.22}$$
$$W_{21} = |W_{21}|e^{i\varphi}. \tag{2.23}$$

Now we consider the dynamical aspect of this problem by using perturbation theory.

Let

$$|\phi(t)\rangle = a_1(t)|\varphi_1\rangle + a_2(t)|\varphi_2\rangle \tag{2.24}$$

be the state vector of the system at time instant t. The evolution of $|\phi(t)\rangle$ in the presence of the coupling is given by the Schrödinger equation.

$$i\hbar\frac{d}{dt}|\phi(t)\rangle = (H_0 + W)|\phi(t)\rangle \tag{2.25}$$

After projecting this equation onto the basis vectors φ_1 and φ_2, and setting $W_{11} = W_{22} = 0$ - without loss of generality, we obtain

$$i\hbar\frac{d}{dt}a_1(t) = E_1 a_1(t) + W_{12}a_2(t)$$
$$i\hbar\frac{d}{dt}a_2(t) = W_{21}a_1(t) + E_2 a_2(t) \tag{2.26}$$

These equations constitute a system of coupled linear differential equations, and it can be shown that it results in a solution, expressed in the new basis $|\varphi_+\rangle$ and $|\varphi_-\rangle$,

$$|\phi(t)\rangle = e^{i\varphi/2}\left[\cos\frac{\theta}{2}e^{-iE_+t/\hbar}|\varphi_+\rangle - \sin\frac{\theta}{2}e^{-iE_-t/\hbar}|\varphi_-\rangle\right], \tag{2.27}$$

where we have used the initial condition

$$|\phi(0)\rangle = |\varphi_1\rangle, \tag{2.28}$$

thus assuming the system being in state $|1\rangle$ at $t = 0$. By using equations (2.20) and (2.21), the probability amplitude of finding the system at time t in the state $|\varphi_2\rangle$ is then written as

$$\begin{aligned}\langle\varphi_2|\phi(t)\rangle &= e^{i\varphi/2}\left[\cos\frac{\theta}{2}e^{-iE_+t/\hbar}\langle\varphi_2|\varphi_+\rangle - \sin\frac{\theta}{2}e^{-iE_-t/\hbar}\langle\varphi_2|\varphi_-\rangle\right] \\ &= e^{i\varphi/2}\sin\frac{\theta}{2}\cos\frac{\theta}{2}\left[e^{-iE_+t/\hbar} - e^{-iE_-t/\hbar}\right] \end{aligned} \tag{2.29}$$

With the probability of the system being in state $|2\rangle$, after initially starting from $|1\rangle$, $P_{12}(t) = |\langle\varphi_2|\phi(t)\rangle|^2$, we obtain [10]

$$\begin{aligned}P_{12}(t) &= \frac{1}{2}\sin^2\theta\left[1 - \cos\left(\frac{E_+ - E_-}{\hbar}t\right)\right] \\ &= \sin^2\theta\sin^2\left(\frac{E_+ - E_-}{2\hbar}t\right). \end{aligned} \tag{2.30}$$

Equations (2.29) and (2.30) are just $a_2(t)$ and $a_2^2(t)$, respectively. After using (2.19) P_{12} can be rewritten as

$$P_{12}(t) = \frac{4|W_{12}|^2}{4|W_{12}|^2 + (E_1 - E_2)^2}\sin^2\left[\sqrt{4|W_{12}|^2 + (E_1 - E_2)^2}\frac{t}{2\hbar}\right], \tag{2.31}$$

which is also called Rabi's formula. Hence we find a two-level system oscillating between the two new states E_+ and E_- - due to light-matter interaction, with its new unique Bohr frequency $\frac{E_+ - E_-}{\hbar}$.

Now we consider the interaction W_{12} itself and will use a dipole approximation of the particle that represents the matter. Since the only states in quantum dots are of excitonic nature, the dipole approximation can be considered to be sufficiently accurate. The necessary two-level system e.g. consists of an exciton state $|1\rangle$ and a no-exciton state $|2\rangle$. The strength of the electrical field component of the exciting light can be written as

$$\vec{E}(\vec{r}, t) = \vec{E_0}(\vec{r})\cos(\omega_L t). \tag{2.32}$$

The polarization of the dipole representing the exciton is in the form of

$$\vec{D} = \vec{d}_{12}(|1\rangle\langle 2| + |2\rangle\langle 1|), \tag{2.33}$$

where 1 and 2 indicate the use of the original set of basis functions φ_1 and φ_2, respectively, and

$$\vec{d}_{12} = -e\langle 1|\vec{r}|2\rangle \tag{2.34}$$

defines the polarization of an electron with the two possible energy states $|1\rangle$ and $|2\rangle$, where e denotes the electric charge of an electron. This definition is rather intuitive, since the electron is able to become manifest in the respective wavefunctions associated with the states $|1\rangle$ and $|2\rangle$. The Bra-Ket operation of equation (2.34) just evaluates the center of mass, thus the "mean" location of the product function of the states $|1\rangle$ and $|2\rangle$, respectively. Since this place is associated with $\vec{r}$, it places a charge at a certain distance

from the location $\vec{r}$, thus representing a polarized matter. Furthermore, if we assume this dipole is located at the origin, the complete interaction Hamiltonian will become

$$W_{12}(t) = -\frac{\vec{D} \cdot \vec{E}(\vec{0}, t)}{2}. \tag{2.35}$$

As we can see, W_{12} is no longer a constant, but depends on t. This, of course, changes the set of coupled differential equations (2.26) and leads to a slightly changed version of equation (2.31), where $E_1 - E_2$ - that is $\hbar\omega_0$, is replaced by $\hbar(\omega_L - \omega_0)$. The 2 in the denominator is simply due to the fact, that $\cos(\omega_L t) = \frac{1}{2}(e^{j\omega_L t} + e^{-j\omega_L t})$. Since we are only interested in the absolute magnitude of W_{12}, it is then rewritten as

$$|W_{12}(t)| = \frac{\vec{d}_{12} \cdot \vec{E}(\vec{0}, t)}{2}. \tag{2.36}$$

If we introduce

$$\Omega_1 = \frac{\vec{d}_{12} \cdot \vec{E}_0(\vec{0})}{\hbar}, \tag{2.37}$$

which is the Rabi frequency of the system, and apply the changes from above, equation (2.31) finally becomes [21]

$$P_{12}(t) = \frac{\Omega_1^2}{\Omega_1^2 + (\omega_L - \omega_0)^2} \sin^2\left[\sqrt{\Omega_1^2 + (\omega_L - \omega_0)^2}\frac{t}{2}\right]. \tag{2.38}$$

What we see is an oscillation between the states $|1\rangle$ and $|2\rangle$ with a frequency depending on the strength of the electric field E_0, the dipole moment d_{12} and the frequencies of the laser ω_L and the one due to the intrinsic energy levels E_1 and E_2, ω_0. Once we excite our original system resonantly, i.e. with zero excitation detuning, or $\omega_L = \omega_0$, we eventually obtain

$$P_{12} = \sin^2\left(\frac{\Omega_1 t}{2}\right), \tag{2.39}$$

leaving an oscillation with the Rabi frequency. Fig. 2.10 illustrates this functional relation, where the pulse area Θ is again introduced as

$$\Theta = \int_{-\infty}^{\infty} \Omega_R(t)\, dt, \tag{2.40}$$

and

$$\Omega_R(t) = \frac{\vec{d}_{12} \cdot \vec{E}_0(\vec{0}, t)}{\hbar} \tag{2.41}$$

incorporates temporal fluctuations of the electrical field amplitude E_0. Equations (2.40), as well as (2.41) give rise to an understanding of Rabi oscillations beyond continuous wave excitation. If the amplitude of the electrical field $E_0(t)$ only differs from zero in a certain range of time, a pulse is defined - having a distinctly associated pulse area according to equation (2.40). To increase it, both the amplitude of the exciting pulse

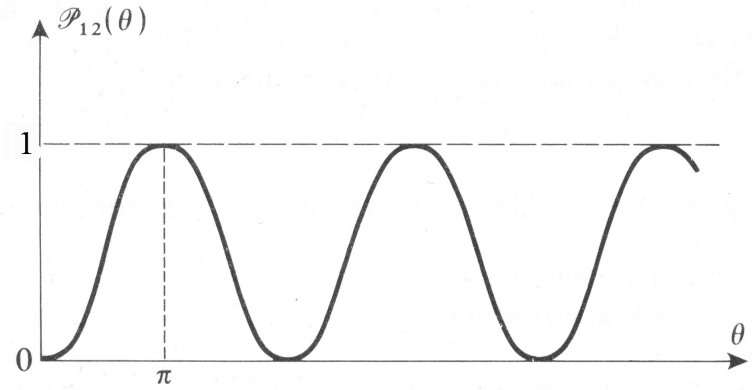

Figure 2.10: Rabi oscillations - the periodic population inversion as a function of the pulse area Θ without damping [10].

and the temporal duration can be raised. In a real quantum dot system, as mentioned before, the polarization of the exciting light is linear and has to be parallel to the excitonic dipole alignment in order to obtain maximum possible excitation. Hence, the inner vector product of equation (2.37) reduces to a simple multiplication and can be used to extract the dipole moment via Rabi oscillation measurements [21] [22].

2.5.2 Rabi Oscillations in Quantum Dots

As already indicated, the excitonic system of a quantum dot constitutes a two-level system, as long as the excitation energy is less than the one of higher excited states and biexcitonic effects can be ignored. Due to the loss of phase coherence, the oscillations are damped. Dephasing mechanisms have already been described in the preceding section. However, according to [23], the major contribution to dephasing in single quantum dots seems to be the excitation induced Coulomb scattering. Like other nonlinear effects Rabi oscillations need a certain excitation power density to be observable. For self assembled InAs - GaAs quantum dots this excitation threshold is about 20 kW/cm^2 [21].

One of the biggest drawbacks of self assembled dot structures is their uneven size. The lateral diameter of the dots is randomly distributed with a Gaussian probability density function (pdf). This obviously leads to a very similar distribution of the exciton Bohr radii, thus a considerably big inhomogeneous broadening of the exciton ground state. This is the reason why many optical experiments have been conducted with single dots instead of the broadened dot ensemble. Hence, the very first observations of Rabi oscillations in quantum dots were conducted using single dot spectroscopy [23][21], where e.g. the energy level splitting $\hbar\Omega_1$ due to the light interaction was observed [21].

Since a quantum dot ensemble was investigated here, only the effects of ensemble signal contributions to Rabi oscillations shall be discussed henceforth. To my knowledge there only exists a single paper on Rabi oscillations in a quantum dot ensemble at present, which is why there is not much theory on dephasing mechanisms in dot ensembles. There

are several indications, however, that the distribution of dipole moments, due to the size distribution, is responsible for the damping of the oscillations [24]. Fig. 2.11a) and b) show calculated exciton and biexciton occupation probabilities as a function of the pulse area $\Omega_1 t$ versus the excitation detuning $\omega_L - \omega_0$ for infinite dephasing time, while d) and e) show the same as in a) and b), respectively, for a finite dephasing time of 1.5 ps. The insets c) and d) of Fig. 2.11 show calculated differential transmission signals $\Delta T/T$ for a plane wave (dotted line), a hyperbolic secant profile (dashed line), including biexcitonic effects (solid line) and after averaging over a distribution of dipole moments (thick solid line), for infinite dephasing time and a finite dephasing time of 1.5 ps, respectively.

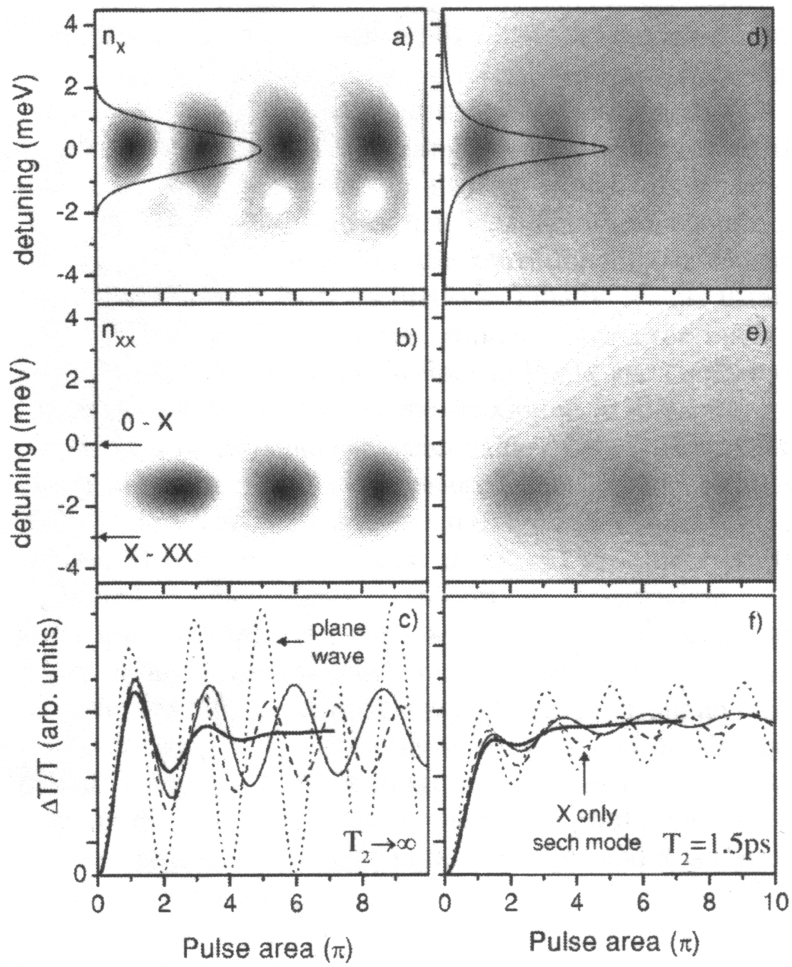

Figure 2.11: Calculated Rabi oscillations as a function of the pulse area Θ for various parameters [24].

Chapter 3

Experimental Methods

3.1 Basic Principles of Selected Spectroscopical Techniques

This section provides an overview of techniques used to gain insight on processes within quantum dots using optical spectroscopy. These methods can be divided into two main groups: The first one focuses on single dot spectroscopy, while the second group concentrates on experiments with quantum dot ensembles. Since this thesis only focuses on the latter group, there will only be considerations of quantum dot ensembles.

3.1.1 Photoluminescence- and Photoluminescence Excitation Spectroscopy

A very intuitive way to characterize processes within a quantum dot is to optically excite the sample and record the excitation induced luminescence spectrum. If the excitation energy is fixed, and the resulting luminescence spectrum is recorded, it is called photoluminescence spectroscopy (PL). Once the spectral scanning position is fixed at the ground state transition, and the excitation source is tuned, the method is called photoluminescence excitation spectroscopy (PLE).

As indicated in fig. 3.1 (a) the energy of the excitation for the PL measurement is fixed at a position above the energy gap of GaAs, which ensures excitation in GaAs only. After excitation, relaxation processes will drive a fraction of the originally excited carriers into the wetting layer, followed by further relaxation into the dots, where they are trapped, until recombination to the quantum dot ground state occurs. A result from such a measurement has already been presented in fig. 1.2 of chapter 1.1 .

It should be noted, however, that the data shown comes from single quantum dot measurements - indicated through the prefixed μ, that stands for micro, on the y-axis labelling. For ensemble PL measurements all observed luminescence lines would appear inhomogeneously broadened, due to the size variations of the self-assembly process. If the excitation power is small enough, so that only one exciton per dot exists, the PL data would reveal the inhomogeneous broadening of the excitonic states within the sample - when measured at low temperature. PL measurements have been performed on the

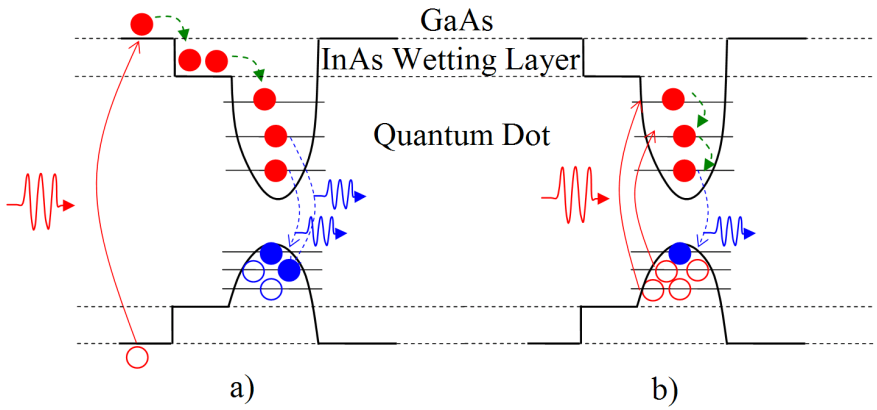

Figure 3.1: Principle of PL a) and PLE b)

sample that has been used for this thesis, and figures will be provided in the next section.

The PL measurement itself reveals all the possible optical transitions within the dot structure, thus, the emission spectrum, whereas the PLE method roughly provides information about absorption and relaxation. If the spectral position of the detector is fixed at the ground state transition, the excitation source is tuned to higher excited states resonantly. So the detector can only observe a signal after relaxation processes between excited states - see fig. 3.1 b), hence, relaxation and absorption is revealed. To classify a quantum dot system through optical excitation, the emission spectrum, as well as the absorption spectrum have to be measured, since these two generally differ from each other.

3.1.2 Spectral Hole Burning Spectroscopy

This well known technique was used in this thesis. Unlike PL measurements, spectral hole burning spectroscopy (SHB) is able to resolve time dependencies without additional instrumentation, when used with a pulsed laser system. Another major advantage of SHB over PL and PLE, respectively, is the ability to determine energy differences in inhomogeneously broadened samples, that are much smaller than the inhomogeneous linewidth, which is why it was preferred over PL and PLE.

The basic principle of SHB is to excite the system under test with a continuous wave laser beam or an ultrashort pulse, that is called pump. The excitation of the system causes - depending on the strength of the excitation, a population shift.

So far SHB measurements are not different from PL measurements. The major difference, however, is the way this population shift is detected. A second, low power continuous wave laser beam or ultrashort pulse gets partially absorbed by the excited sample, depending on the excitation, thus “probes” the state of population. This is the reason why SHB is also sometimes referred to as a “pump-probe” technique. This principle is shown in fig. 3.2, where a) demonstrates how the inhomogeneous linewidth is given by the simultaneous occurrence of many homogeneous lines, while part b) indicates a spectral hole. The spectrally narrow pump pulse (red) causes an induced transmission enhancement

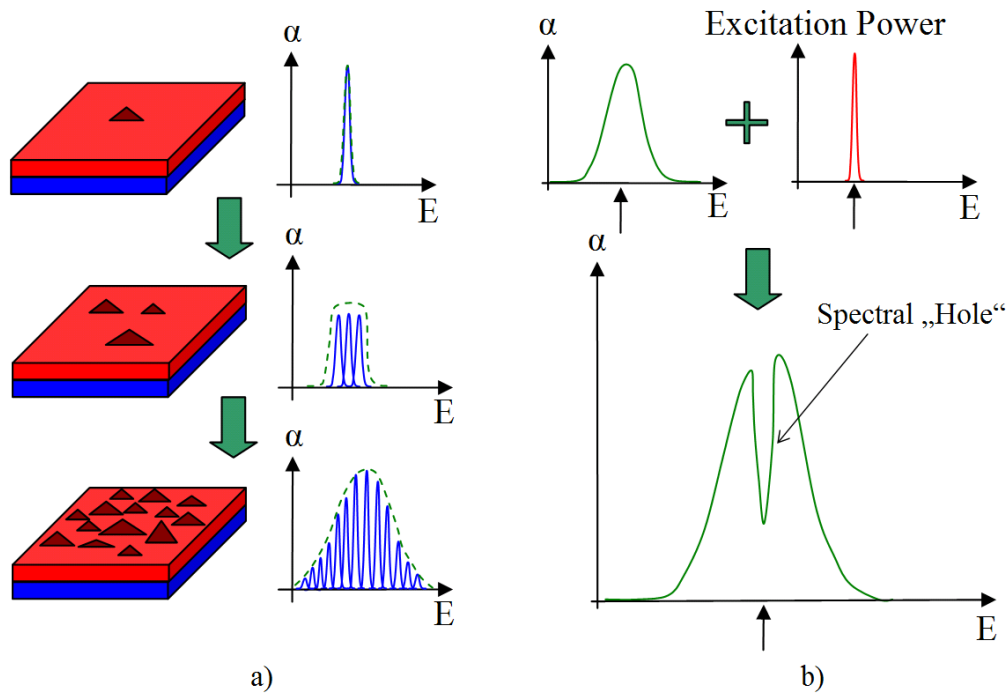

Figure 3.2: The emergence of the inhomogeneous linewidth due to size variations in a), and a distinctive hole in the inhomogeneously broadened absorption, that has been "burned" through the pump pulse in b).

at its spectral position. If absorption (α) is plotted instead of transmission, the name spectral "hole" becomes clear.

In the case of continuous wave beams for both, pump and probe, the pump pulse is spectrally fixed, while the probe pulse is detuned in an adjacent spectral region around the pump frequency. For SHB, using ultrashort pump and probe pulses, the detuning of the probe pulse is not necessary, since it provides an intrinsic broad spectrum associated with the ultrashort laser pulses via Fourier transform properties. The bandwidth of the pump pulse is determined by the used setup. While a continuous wave source almost provides an arbitrarily narrow spectrum - with the total loss of temporal resolution - an ultrashort pump pulse is able to perform in a system where a temporal resolution is required, but with a comparably broad spectrum. All these considerations lead to a tradeoff between temporal and spectral resolution given by the Fourier transform and the measurement requirements. If the energy of the pump pulse is the same as the the one for the probe pulse, it is called a "degenerate" pump/probe measurement.

If one wants to perform time-resolved measurements using PL techniques, an additional detector, a so called streak camera, must be used, that also has to be synchronized with the pulsed laser system, or a photoluminescence up-conversion spectroscopy is used. This technique uses ultrashort laser pulses to excite the sample and then combines the emission of the dot with the same pulses with adjustable time offset, to induce wave mixing in a second order nonlinear material. The signal must then be extracted from a spectrally shifted position, that is where the name up-conversion comes from.

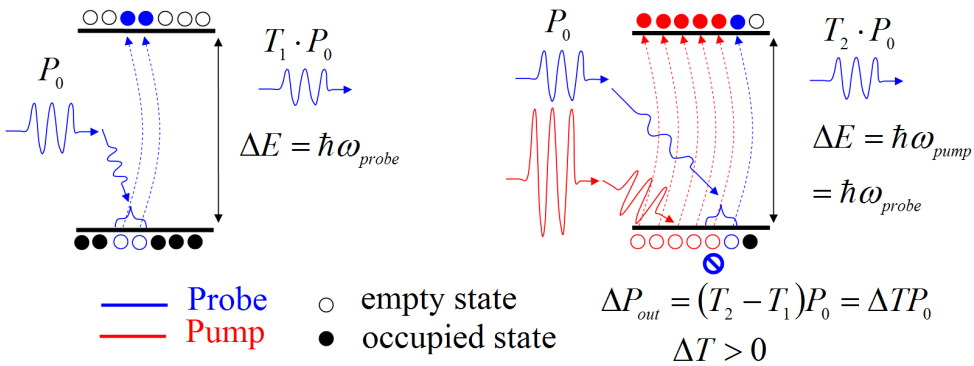

Figure 3.3: The spectral hole burning technique I: A resonant pump pulse ($\Delta E = \hbar\omega_{pump}$) induces an enhanced transmission $\Delta T \geq 0$ of the probe pulse ($\Delta E = \hbar\omega_{probe}$) through both, ground state bleaching and final state blocking.

Fig. 3.3 shows the principle of a SHB - measurement. Since this thesis is about time resolved measurements, the probe and pump fields will only be referred to as probe and pump pulses, respectively. As the left side of the picture indicates, without the pump pulse perturbation, the probe pulse gets partially absorbed, hence, leaving a certain amount of transmitted power of the probe pulse $T_1 P_0$. If the pump pulse excites the system shortly before the probe pulse is transmitted, we are dealing with a different absorption/transmission situation. Since there is a limited amount of carriers and, hence, states available, the pump pulse can bleach the number of ground state carriers - leading to a fewer number of carriers available in the ground state. Hence, the probe pulse will pass this area with fewer absorption taking place, and the transmitted power will increase to $T_2 P_0$. This would be the case for pump induced transmission enhancement, resulting in a positive value of ΔT, or, equivalently, in a spectral hole.

Fig. 3.4 shows the second possible scenario. A three level system with two different excitation energies between the two adjacent states - like the excitonic energy structure in a quantum dot, see fig. 2.5, is pumped with an energy ΔE_2. This populates the initially empty excited state. Once a probe pulse with energy ΔE_1 is passed through this system, it is able to populate the higher second excited state. Hence, this would be the case, where the pump pulse induces an absorption enhancement. Since the sign of ΔT is opposite, compared to a spectral hole, this case is also called the spectral anti-hole.

This is the reason, why SHB spectra can include positive and negative signal contributions. Usually the signal ΔT is normalized with respect to an arbitrary T to include all the measurement system uncertainties. Since a pulsed laser system is presumed, the spectra of both, pump and probe pulse, are considerably broad. If the pump pulse in the second scenario is tuned just at ΔE_2, without having spectral components at ΔE_1, the much broader probe pulse must be set to incorporate spectral components at both energies, ΔE_1 and ΔE_2. After detecting the respective probe components with a spectrometer, the positive and negative signals can be resolved individually.

The reason, why only differences between transmissions with an active pump- and

inactive pump pulse are measured, is the necessity of a detection scheme. In order to detect the probe pulse's change in transmission only the probe pulse has to be routed into the detection device (spectrometer). As already mentioned, the number of carriers in a dot sample are limited, thus the number of photons, interacting with them, is limited as well. This small amount of photons is the only signal one is interested in, making all other probe related signal components, not caused by the pump pulse, a contribution to the overall noise in the system. This ultimately leads to the problem, that a direct measurement of the desired signal is practically impossible.

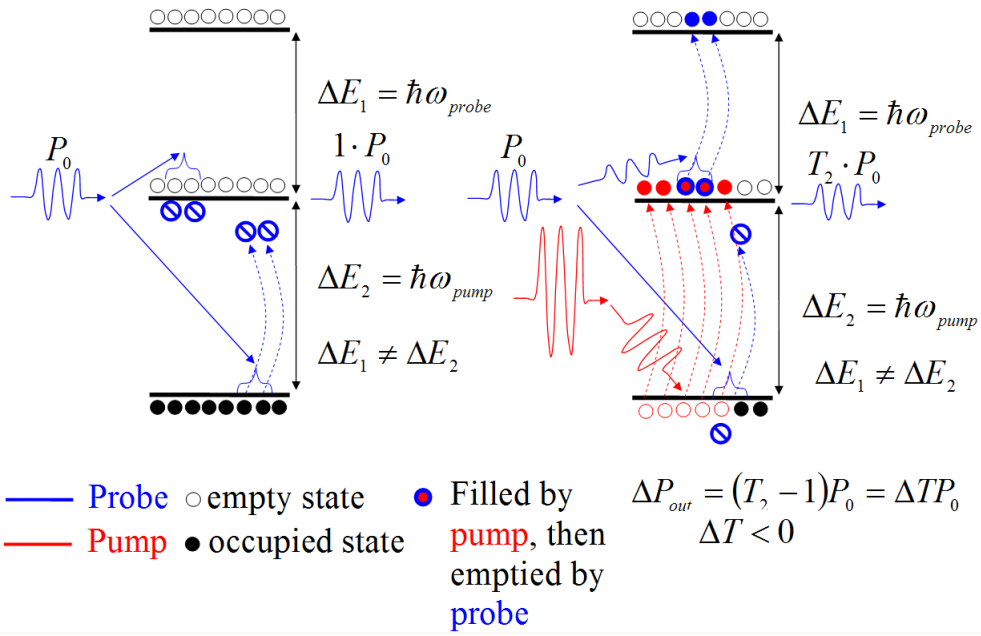

Figure 3.4: The spectral hole burning technique II: A resonant pump pulse ($\Delta E_2 = \hbar\omega_{pump}$) induces an enhanced absorption $\Delta T \leq 0$ of the probe pulse ($\Delta E_1 = \hbar\omega_{probe}$) in two steps. At first, the pump pulse populates the first excited state, and then, secondly, the probe pulse gets partially absorbed via the ΔE_1 transition.

The solution to this problem is the introduction of a lock-in detection scheme. This well known technique purposely modulates the input signal (pump) of the desired system under test with a certain frequency, and then only detects signal components of the output signal (probe) in a certain bandwidth around this modulation frequency, thus significantly cutting down on the noise bandwidth and ignoring all output signal components not caused by the input signal.

This also applies for optical measurement systems, where the modulation of the pump signal is performed by either an acousto-optic modulator or a simple chopper. The latter one was used for the measurements in this thesis. So the modulation used for the detection scheme infers an alternating pump signal, eventually leading to the differential transmission signal.

3.2 The Femtosecond Laser System

For this thesis a mode-locked Ti:Sapphire LASER has been used to provide pulses only 80 fs long, repeating with 80 MHz. This corresponds to a spectral width of approximately 10 nm full width at half maximum (FWHM), or, equivalently 15 meV FWHM. Fig. 3.5 shows actual measurement data of the laser spectrum.

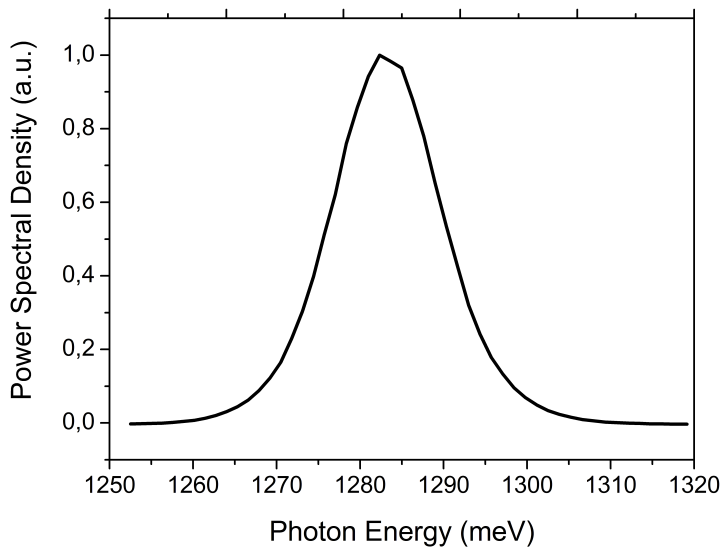

Figure 3.5: Power spectral density versus photon energy of the laser system used for the experiments

In order to provide ultrashort laserpulses in the femtosecond range, there have to be certain conditions on the system. Firstly, the material of the active region in the laser has to provide a certain gain bandwidth, and then, secondly - once the first point is met, all the continuous wave modes in the spectral region have to have a certain phase relation to each other. This is called "mode-locking" and can either be actively or passively. The Ti:Sapphire laser system a priori provides the necessary bandwidth and can be actively set into a mode-locking state with an acousto-optic modulator.

Fig. 3.6 provides an overview of the beam paths within the femtosecond laser system used as a coherent photon source in this thesis. Prisms Pr2 and Pr3, in combination with the tuning-slit, allow a selection of the center wavelength, by only enabling certain wavelengths to pass the slit. Since these prisms introduce a certain amount of dispersion, that depends on the wavelength, the length of this part of the beam path has to be adjusted accordingly to cancel the dispersion. The Ti:Sapphire rod is the active lasing material, providing a broad spectral range of gain, and is pumped optically with the pump beam (5 W continuous wave at 532 nm). AOM indicates the position of the acousto-optic modulator, that is responsible for the active mode-locking. It has to ensure a phase correlation between the continuous wave modes lasing in the cavity. If this relation is established, mode-locking is enabled and constructive interference of all the modes occurs only within the few femtoseconds that define the duration of the pulse.

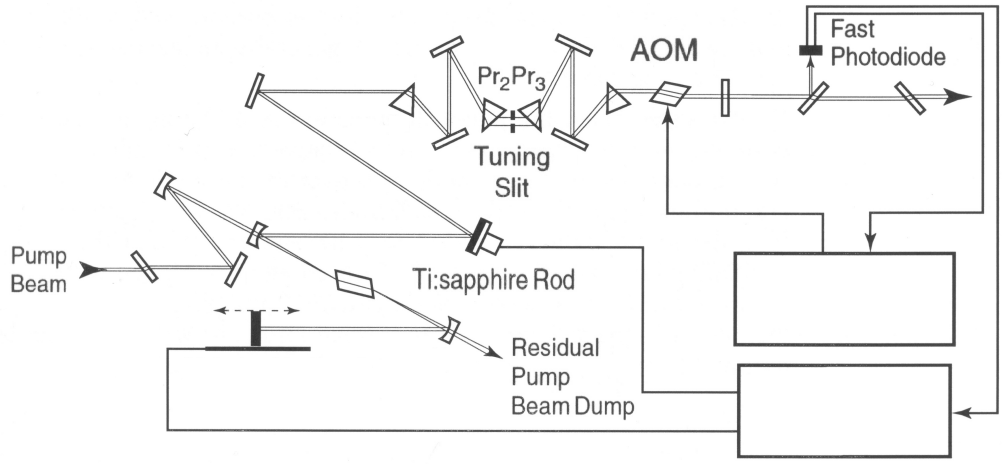

Figure 3.6: Beam path within the cavity of the actively mode-locked Ti:Sapphire femtosecond laser used in this thesis.

The desired wavelength for the experiments was about 965 nm which gave rise to the use of the appropriate mirror set - ranging from 840 nm to 1000 nm. These sets are designed for optimized output power within their specified wavelength range.

3.3 Femtosecond Pulse Shaping

As already indicated, the spectral hole burning technique, as well as excitation in general, relies on spectrally well defined laser sources, and there is a Fourier limited tradeoff between the temporal and the spectral dimension, which has to be adapted to the measurement requirements. In order to provide selected excitation of the states of interest (excitons), without interfering with other states - like biexcitons - the bandwidth of the pump pulse is upper bound. As the biexciton's binding energy is approximately 4 meV, this constitutes the upper bound for measurements in this thesis. Since the pulsed laser system, described in the previous section, provides a comparably broad spectrum (15 meV FWHM), the pump pulse needs to be spectrally shaped, before it can serve as an excitation source. Fig. 3.7 shows a common way to implement spectral shaping [25]. The femtosecond input pulse is routed to the left grating with such an angle, that results in a collinear alignment of diffraction order -1 and the horizontal lens-mask-lens axis. The left grating provides the necessary wavelength - spatial coordinate transformation, while the left lens is responsible for a distinct separation of the spectral components at its focus. The very reason for this arrangement is, because the incoming beam has a finite profile, thus leading to a spatial overlap of different spectral components, depending on the position observed. Only after putting a lens into the system, all spectral components can be resolved individually at its focus. It should be noted that the focal point is the only point, where all spectral components are spatially disjoined.

The straight line, determined by the focal points corresponding to increasing/decreasing wavelengths, is the optimum place for the shaping mask. For the experiments performed

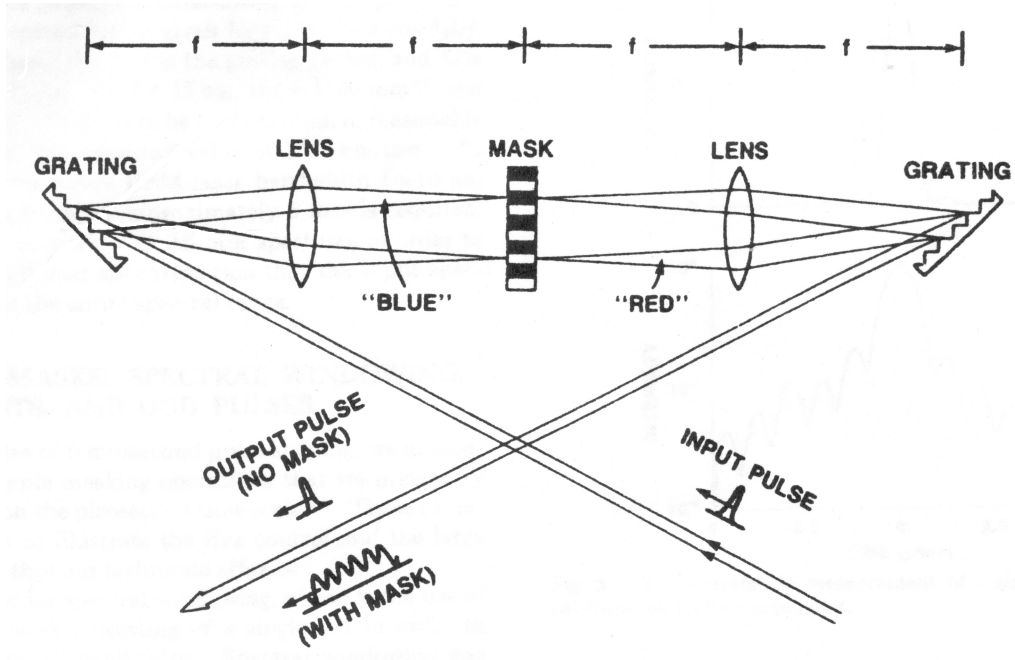

Figure 3.7: Spectral pulse shaping in the spatial domain through wavelength $\longrightarrow$ space $\longrightarrow$ wavelength transformation [25].

in this thesis, the shaping mask only consists of a slit, where position and slit width are adjustable. Hence, this system constitutes an example for an ideal bandpass, which would be non-causal. However, since lenses are not ideal, thus having a finite focal profile, and the slit forms an aperture, that results in diffraction at its edges - that influence the signal strength at the lens, even for dimensions bigger than the corresponding wavelengths, the pulse shaper deviates from its ideal theoretical counterpart.

The only important (focal) lengths f are the ones between the first lens and the spectral mask, and the second one between the second lens and the second grating, respectively. The other two lengths, having same dimension f, are due to symmetry considerations.

It should be noted, that a mask with a dispersion free media always causes a real valued "transfer function", since it does not affect the phase of the spectral components. So only a dispersive material, where ϵ is a function of the frequency, is able to shape a pulse in magnitude and phase. Furthermore, progressive reduction of the slit's width, and hence, the spectral width of the pulse, inevitably leads to an increase of the pulse's temporal length, due to the Fourier transform properties.

The lenses used for the pulse shaper had a focal length f of 15 cm, and the grating provided a parameter $1/d$ of 1800 lines per mm, where d is the grating period and a diffraction angle θ_d of approximately 79°. This leaves a spectral resolution of the pulse shaper of [25]

$$\frac{\delta\lambda}{\delta x} = \frac{d\cos(\theta_d)}{f} \approx 0.7 \text{ nm/mm}. \tag{3.1}$$

3.4 The Grating Spectrometer

The device used for signal detection - the grating spectrometer, is shown in Fig. 3.8. The basic principle is similar to the one of the pulse shaper, since it also uses a grating for a wavelength $\longrightarrow$ space transformation. At first the parallel beam of the probe pulse is

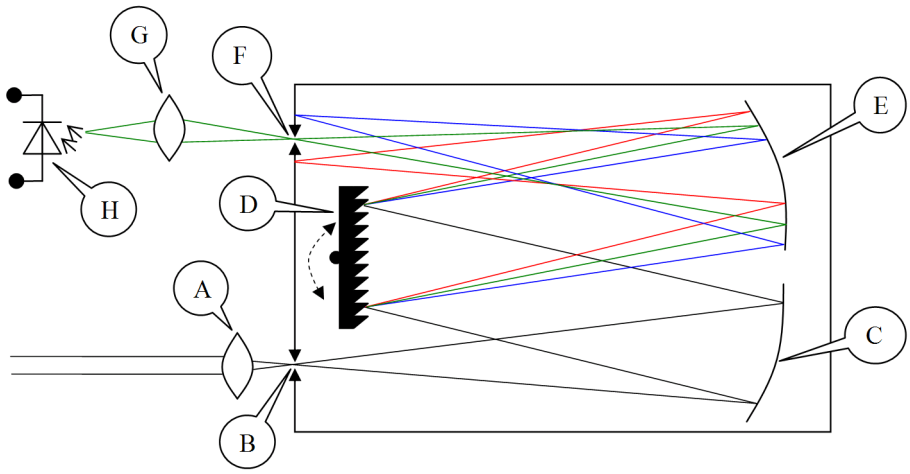

Figure 3.8: Basic functionality of the grating spectrometer used for the experiments.

focused with lens (A) through slit (B), placed exactly in the focus. The focal length f of lens (A) was 35 mm. So the width of slit (B) should only be limited by the focal profile. Within the spectrometer, the widened beam lights most of the spherical mirror (C), and providing a parallel beam after the reflection. The rotatable grating (D) is responsible for the wavelength selection, since spherical mirror (E) focuses only a certain beam angle directly through slit (F). This is indicated through the splitting of "white" light - through the grating, into it's respective components "blue", "green" and "red" with only one wavelength component - in this case the "green" one, being able to pass through slit (F). The characteristic length of the spectrometer used for the experiments in this thesis - the length of the beam path between the grating and mirrors (C) or (D) was 75 cm.

As one can imagine, the width of slit (F) determines the resolution of the spectrometer - the smaller the width, the better the resolution, but the smaller the signal strength, since the power spectral density is roughly constant.

Once the beam passed the output slit, there is one more lens (G) to focus the beam into the photodetector (H), that is usually a simple photodiode. As the wavelengths of interest for the experiments in this thesis are 965 nm, a regular silicon-based p-n photodiode was used for detection. Since the photocurrent is proportional to the power, it provides a direct measure of power (density) at the respective wavelength. After converting the photocurrent into a voltage, e.g. with an I/V amplifier, lock-in detection can then be performed on the electrical signal. The chopper used for the modulation of the pump provided a modulation frequency of 2 kHz, that was used as the reference for the lock-in detection.

3.5 Temporal Alignment between Pump and Probe

In order to perform time resolved measurements, i.e. to determine the spectral hole burning response x ps after the arrival of the pump pulse, the beam paths between the pump and probe pulses have to match their respective lengths within an accuracy of μm (1 ps $\triangleq$ 300 μm). This is done by initially aligning the setup - see below - within an accuracy of 1 cm, and then, using a motorized translation stage to obtain the exact position. It should be noted that, of course, not only a temporal alignment of pump and probe must be established, but also a spatial alignment - to only probe the area under excitation. This procedure, however, is comparably simple and is done by a direct observation on a monitor, that is feeded by a camera with an appropriate near infrared objective and a common silicon-based CCD sensor array. Since the photon energy of the pulsed laser system - at 1280 meV - is still big enough to create electron-hole pairs within the CMOS cell of the charge-couple device, a display is directly possible, revealing the positions of both, the pump and the probe beam at a scattering surface - the sample.

As already indicated, the SHB signal depends on the excitation - the pump. This infers a direct usage of this signal to find a temporal alignment between pump and probe, since probing after excitation will definitely result in a different signal than probing before the excitation with the pump.

So if the beam path of the probe pulse is shorter than that of the pump pulse, thus, the sample is probed before it has been excited, there should not be any change in the transmission signal. Hence, $\Delta T = 0$ for $t < 0$. Once the pump pulse is able to excite the sample before the probe pulse arrives, then, of course, a change in the transmission signal occurs, leaving a characteristic "step" function located exactly at the temporal overlap. The slope of this step is obviously determined by the duration of the pump pulse, which is in the order of picoseconds.

If the excitonic state, induced by the pump pulse excitation, is maintained even after the pump pulse is already gone, the differential transmission signal can be maintained as well, thus keeping the step from returning to zero. As already indicated, excitonic states in a quantum dot are prone to decoherence and relaxation through phonons. Hence, the signal to noise ratio (SNR) strongly depends on the temperature. This is why all "steps" in this thesis have been measured at 5 K. Fig. 3.9 shows actual measurement data of this characteristic step - function, for both , the excitonic (b) and the biexcitonic (a) transitions. The reason for these distortions at the excitonic transition is the interference of the probe with the reflection of the pump. The beam splitter used to separate probe and pump determines the ratio of the powers between them - in the case of this setup $P_{pump}/P_{probe} = 4\%$. This value is very close to the reflection coefficient of lenses, cryostat windows or the sample.

So a single reflection of the pump pulse still leaves a signal in the same order of the original probe pulse. Since the excitation (pump) and the (probed) excitonic transition are in resonance, this spectral position is prone to interferences - unlike the biexcitonic transition. The biexciton binding energy of approximately 4 meV leads to a distinct spectral shift, and the fact, that the pump pulse does not incorporate any spectral components at this position leads to an observation of the step without distortion - as shown in a).

What fig. 3.9 a) also reveals is a small periodic signal that seems to be superposed

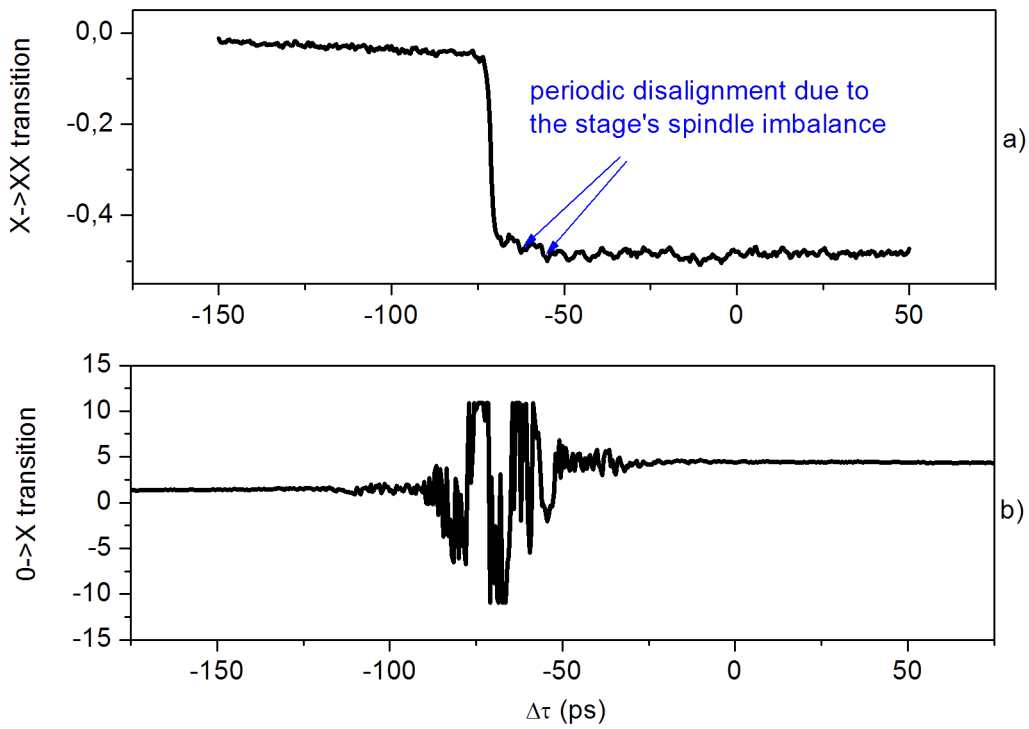

Figure 3.9: Finding temporal alignment between pump and probe by using the SHB signal evaluated at the biexictonic transition a) and the excitonic transition b)

to the SHB signal. The period of this signal is approximately 5 ps - the same value that corresponds to a single full rotation of the motorized translation stage's spindle. This already indicates the origin of this signal component: The spindle of the used stage appears to be somewhat imbalanced, which lead to a periodic disalignment of the probe pulses beam path.

Even if the data of fig. 3.9 b) is corrupted around the point of temporal alignment, it still indicates the existence of the step, since it shows a flat response before and after the artifacts, except with a different magnitude. Since the biexcitonic transition of part a) involves a three-level scenario, depicted in the previous sections, the spectral hole burning response is expected with a negative sign.

3.6 The Quantum Dot Sample

For this thesis a 3×3 mm^2 sample of self-assembled InAs/GaAs quantum dots was used to conduct measurements with. Fig 3.11 shows a cross section of it, revealing 30 layers of the InAs dots, simply to enhance signal strengths for measurements. Each layer provides a dot density of roughly 2×10^{10} cm^{-2}. In order to be accessible by the used Ti:Sapphire laser system the sample has undergone a rapid thermal annealing treatment in a forming gas atmosphere at a temperature of 800°C for 240 s [18]. This eventually leads to an energy shift of the excitonic ground state transition to wavelengths from 900 nm to 1000 nm, which is due to temperature enhanced diffusion processes reforming the dots. At 5

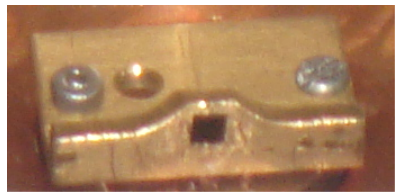

Figure 3.10: The 3×3 mm^2 sample mounted on the sample holder to provide mechanical stability as well as thermal conduction to the cryostat's finger.

K the photoluminescence spectrum provides a significant broadening around the center frequency of 1281 meV. As already mentioned, this mainly comes from the variance in the dot-dimension distribution. Fig. 3.10 portraits the sample, mounted on the sample holder. The GaAs buffer layer is necessary, since the substrate only consists of a polished piece of GaAs with a rough surface - measured in atomic dimensions. Therefore the buffer layer is grown to provide a monolithic smooth surface, where the InAs quantum dots can form themselves.

3.7 The Experimental Setup

After several changes throughout the different measurements the final setup is depicted in fig. 3.12. In order to provide separate pump and probe beams, a beam splitter is used right after the laser source. Henceforth all pump beam paths are red colored, while the probe beam path is provided in blue. The beam splitter itself only consists of a glass plate - approximately 3 mm thick. This leads to a back-reflection guided parallel to the desired probe beam, only a few millimeters apart. To cancel this unwanted beam, a pinhole (1) is placed in the center of the desired probe beam, absorbing everything else.

While the probe pulse is immediately guided to the translation stage (B), the pump pulse passes the pulse shaper (A) first. To equalize the beam paths between pump and probe, the probe pulse has to be routed through the translation stage (B). The preceding sections already dealt with finding the position of the stage, where pump and probe paths exactly match.

For the measurements presented in chapter 5, an adjustable attenuator was used to provide a continuous variation of the pump pulse's power. After passing the attenuator, the pump pulse is routed through the chopper wheel - for lock in detection - and the half-wave plate for polarization dependent measurements, until it is finally being focused along with the probe pulse, through the cryostat's (C) window, right on the sample (D). As indicated in the picture, the focal length of this lens is 3.5 cm. This not only determines the dimension of e.g. the cryostat - placed right after this lens - but also influences the effective diameter of the beam at the focal point, given by the expression [26]

$$d \approx \frac{4\lambda f}{\pi d'}, \tag{3.2}$$

where λ denotes the (center) wavelength of the beam to be focused, f is the focal length of the lens, d' is the diameter of the incoming beam and d is the resulting diameter of the beam in the focus. This equation holds true for a general lens characterized by its

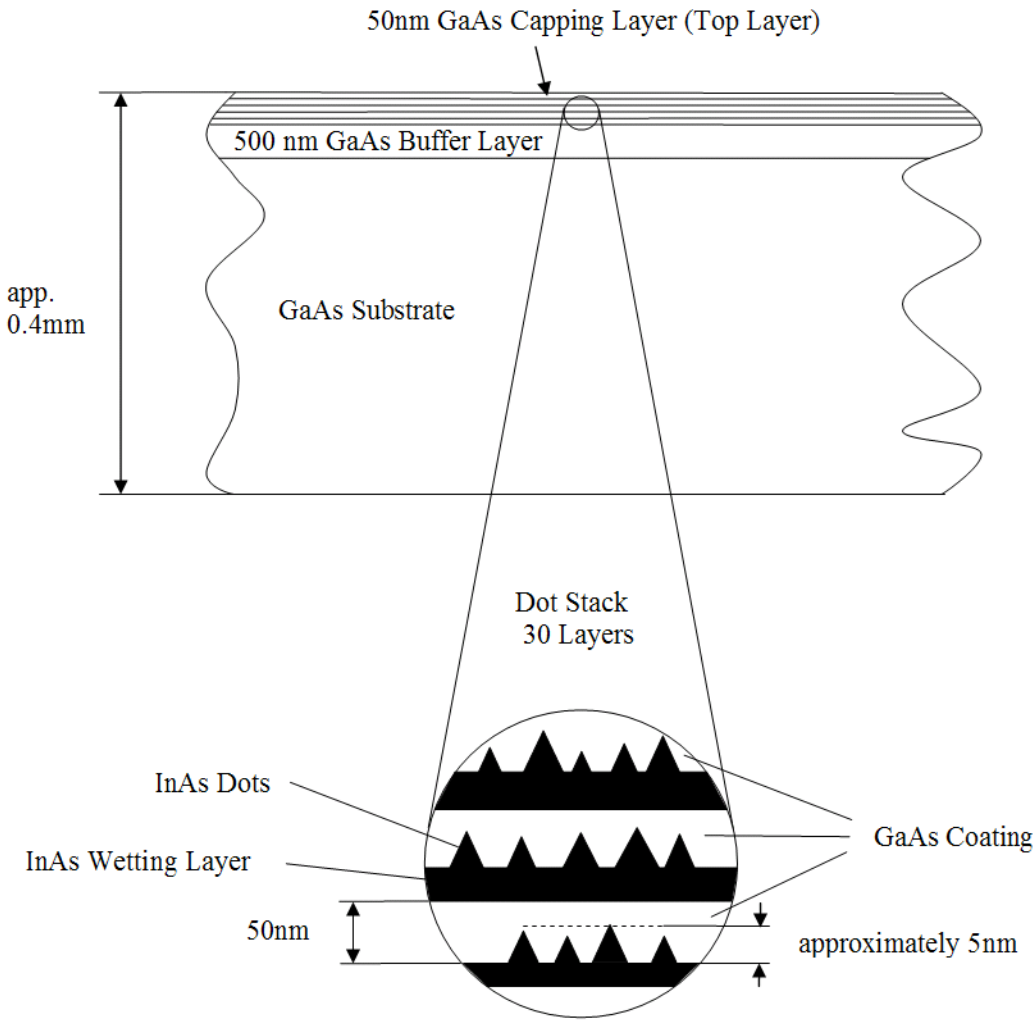

Figure 3.11: Structure of a stack of self-assembled InAs/GaAs Quantum dots used for the experiments.

focal length f. Plugging in the values of this setup ($f = 3.5$ cm, $\lambda = 965$ nm, $d' \approx 2$ mm), results in a focus diameter of $d = 20$ μm. While the transmitted pump pulse is immediately extinguished with an absorbing material, the probe pulse is reconstructed by a lens ($f = 10$ cm) for zero beam divergence, until it reaches the spectrometer to be finally detected.

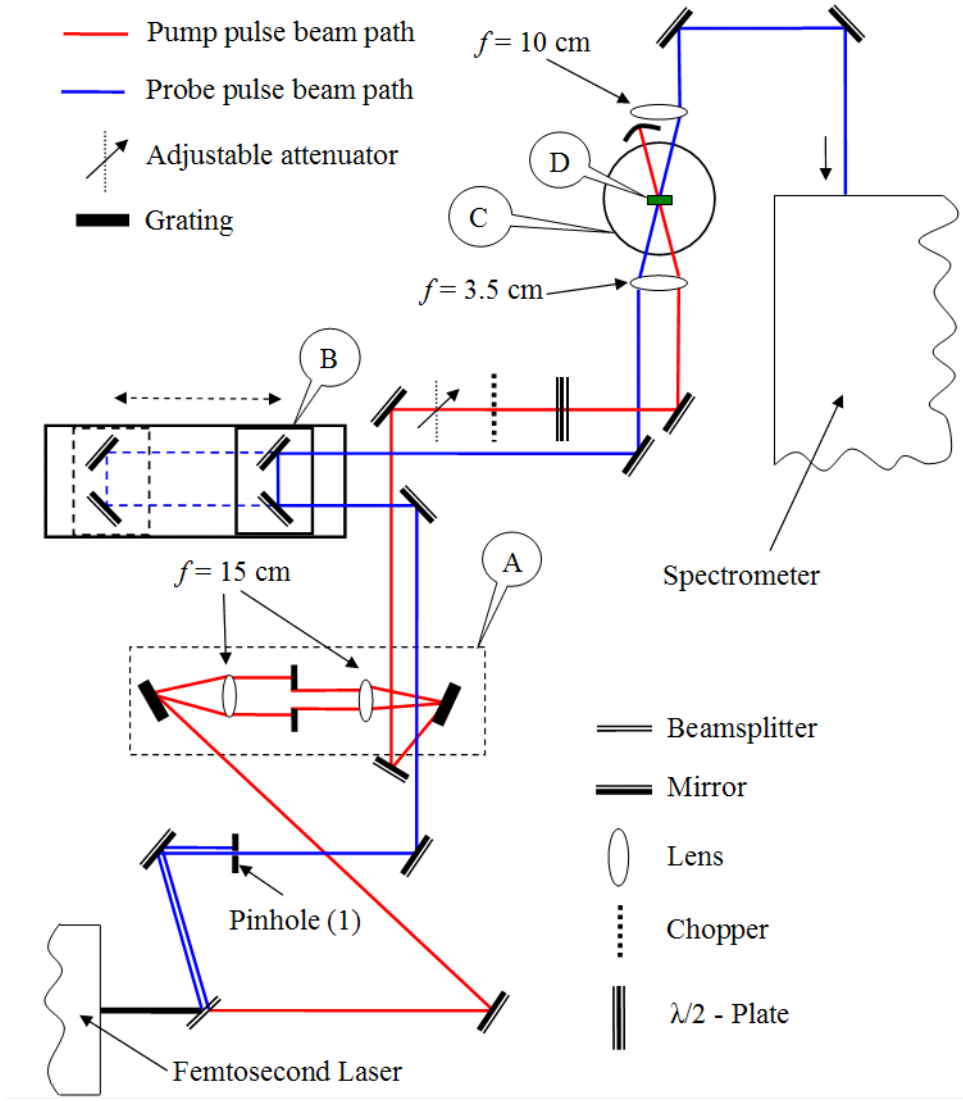

Figure 3.12: The final measurement setup as it was used for the experiments. The functional blocks are: (A) pulse shaper, (B) translation stage, (C) cryostat, (D) quantum dot sample

Chapter 4

Experimental Results - Spectral Hole Burning Spectra

The following chapter provides measurement data with pump pulse areas significantly smaller than π, thus, well below any noticeable effects of Rabi oscillations or other non-linear effects.

4.1 Photoluminescence

To find the optimal excitation wavelength for the spectral hole burning measurements of the sample, the inhomogeneous broadening, thus, the center frequency and the bandwidth around it must be determined first. The most convenient way to to do this is by performing photoluminescence spectroscopy - as already described in detail.

Fig. 4.1 provides the data of preceding photoluminescence spectroscopy measurements, that was already available at the beginning of this thesis. Keeping the energy structure of the harmonic oscillator - as a model for the quantum dot - in mind, the data is explained intuitively. Just like any other system underlying Hund's rule of maximum multiplicity, states in quantum dots also tend to get populated energetically from bottom to top. This infers that an excitation power low enough to create such a limited amount of carriers to only fill the bottom states, would result in a luminescence spectrum like the red curve of fig. 4.1, thus only containing s-shell transitions.

This is already the necessary information needed to find the optimal spectral position and range of the excitation source needed for the spectral hole burning experiments. From this curve one can extract: E_{center}= 1280 meV, ΔE_{FWHM} = 45 meV. This means, that most of the dots in the sample provide a ground state transition energy of 1280 meV, while $\pm\frac{\Delta E_{FWHM}}{2}$ meV apart from E_{center} there are only half as many dots left with ground state transition energies of $E_{1,2} = E_{center} \pm \frac{\Delta E_{FWHM}}{2}$.

The blue curve, however, shows the luminescence spectrum for higher excitation power. In this case, there are too many carriers to just populate the ground state, and Pauli's exclusion principle comes into play, thus leading to the population of the p-shell. What these curves also distinctly show, is the degree of degeneracy of the different shells. The peak luminescence power of the s-transition is almost half as big as the maximum of the p-transition, indicating almost twice as many possible states in the p-shell compared to

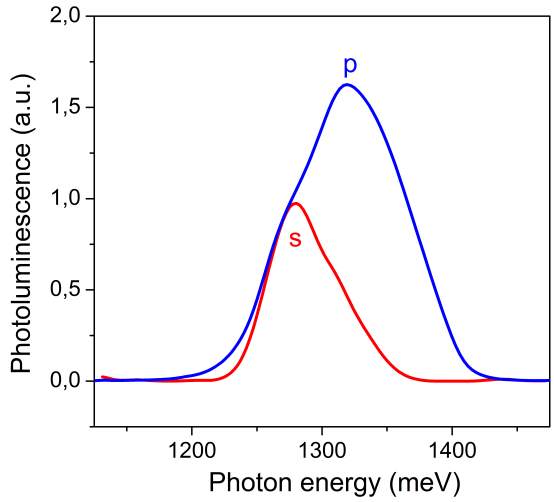

Figure 4.1: Photoluminescence spectroscopy results of the sample used for the spectral hole burning spectroscopy measurements in this thesis. The red line shows data with low excitation power, where the majority of the excited carriers are excitons in the ground state (s-shell), while the blue line indicates s- and p-shell transitions.

the s-shell. If the excitation power would be increased further, the maximum of the p-shell would increase until it is exactly twice as big as that of the s-shell - thus twice as many possible states in the p-shell compared to the s-shell. Then the d-shell becomes populated, without changing the saturating behavior of the maxima for s- and p-shell and so on.

4.2 Polarization and Temperature Dependence

Before each experiment the pump as well as the probe pulse have been measured in order to ensure repeatable results. Since the pulse shaper provides an adjustable width and position of the slit, thus adjustable bandwidth and center frequency of the pump pulse, the excitation of the dots could be determined selectively. Due to the inhomogeneous broadening of the sample and the pump bandwidth being varied between 300 μeV and 4 meV FWHM (full width at half maximum), respectively, only dots within this range of energies were excited. Fig. 4.2 shows the spectra of different pump pulses centered around 1285 meV. In order to compare pump and probe directly, fig. 4.3 shows data of a 350 μeV pump pulse and the probe pulse with 15 meV. It should be noted, that all measurements have been carried out around the maximum of the inhomogeneous broadening of the sample, however, just to observe differences between dots due to size fluctuations, the same experiments have been conducted at the very edges of the inhomogeneous broadening - 1260 meV and 1285 meV, as well. But it turned out that there have been no obvious differences.

As already mentioned, the excitonic states in self-assembled quantum dots are excited with linearly polarized light. To get an $|X_H\rangle$ exciton, one needs to excite with horizontally polarized light, and with vertically polarized light, to obtain the $|X_V\rangle$ exciton. As a

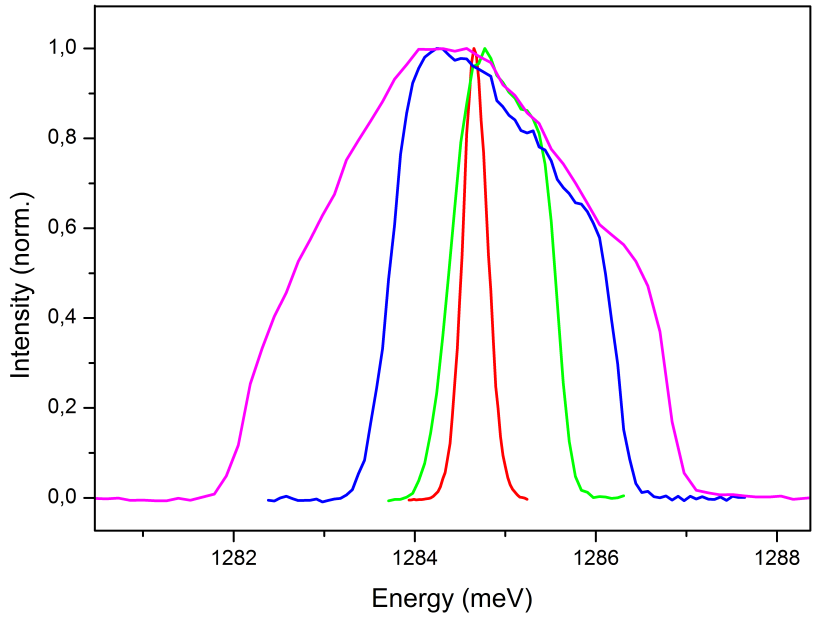

Figure 4.2: A variety of pump pulses differing in bandwidth. All plots are normalized with respect to the maximum signal. The red curve shows a 300 μeV pulse, the green indicates 1 meV, blue stands for 2 meV, while the magenta colored curve shows a 4 meV pump pulse.

consequence the biexciton can only be created out of existing excitons, if the light has the same polarization. This is, as already indicated, due to the existence of a superposition of two original states, created by circularly polarized light. This condition infers, that the probe pulse has to have the same polarization as the pump pulse in order to create a biexciton.

Since relaxation processes tend to flip the spin of excitons, biexcitonic states can also be formed with orthogonal pump and probe pulses, provided a sufficiently large number of excitons have flipped their spin [18]. This, of course, is determined by both the temperature of the sample and the time it is probed after excitation. Provided a certain time t is chosen, and the pump pulse provides the orthogonal polarization to the probe pulse, the number of biecxitonic states should increase with temperature.

Fig. 4.4 reveals the assumptions from above, as well as many other interesting features. The pump-probe delay time t is fixed at 100 ps for all measurements, as well as the excitation bandwidth of the pump pulse at 350 μeV. The temperature is varied from 5 K to 90 K (rows). Both, pump and probe use the same horizontal polarization, indicated by the subscripts H. To map transmission into absorption all measurement data has been flipped vertically, resulting in excitonic holes, denoted by X, and biexcitonic antihole contributions, denoted by XX. The peak amplitudes of the excitonic as well as the biexcitonic transition depend on both, the pump and the probe power.

The creation of a biexciton by the probe pulse is initially enabled and, indeed, all

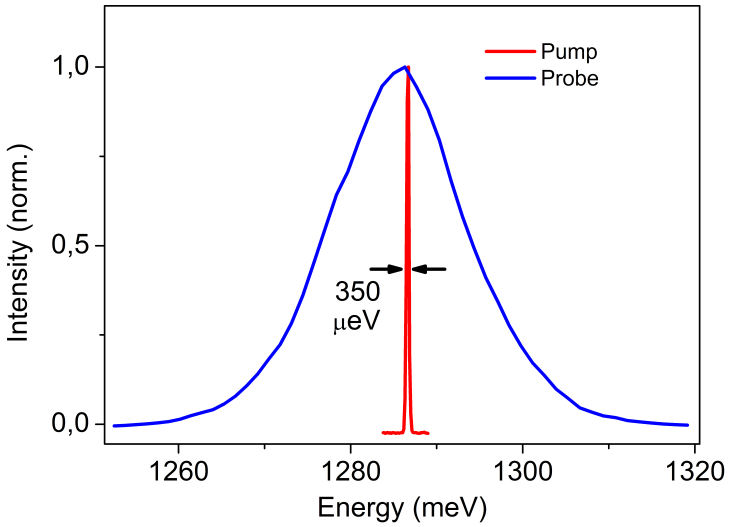

Figure 4.3: Measured pump and probe pulse before beginning the experiments

graphs provide the characteristic smaller antihole approximately 4 meV below the excitonic spectral hole. Even if the spectral position, or the bandwidth of the pump pulse is varied, the energetic distance between the exciton and the biexciton remains almost identical. This means that the biexcitonic binding energy remains always at 4 meV. As already mentioned, this mainly comes from the asymmetry of self-assembled InAs quantum dots.

Another remarkable result, that is best observed at 60 K, is the inhomogeneous zero-phonon line, having 350 μeV FWHM spectral width, surrounded by the broad phonon pedestal. Since this excitation bandwidth is still much bigger than the homogeneous broadening of the zero phonon line of a (selected) single quantum dot (a few μeV), the shape of the excitonic line is determined by the superposition of many single lines - very similar to the overall pump pulse spectrum. The thermal "evolution" of the sidebands verifies the assumptions made to quantify exciton-phonon interactions in chapter 2. Hence, for low temperatures phonon interactions don't even come into play, while they get more and more important with increasing temperature. At 90 K the original zero-phonon line cannot be resolved from the phonon dominated spectrum. As already indicated in fig. 2.7, the energetic range of phonons, being able to interact with excitons, is restricted, leading to a limited bandwidth of phonon-assisted excitonic transitions of approximately 4 meV. This effect can be seen in the temperature range from 60 K and above, where the spectral range of the phonon pedestal stays almost the same.

Fig. 4.5 reveals similar results, with the only difference of orthogonally polarized pump and probe. Since graphs 4.4 and 4.5 provide the same scale, the magnitudes of the excitonic transition in 4.5 shows approximately half the amplitude compared to 4.4. The reason for this effect is an absorption enhancement due to the lack of final state blocking, since the pump pulse bleached the ground state, but only blocked the $|X_V\rangle$ state, whereas the probe pulse only induces a transition to the $|X_H\rangle$ state. Yet another prediction of the

-

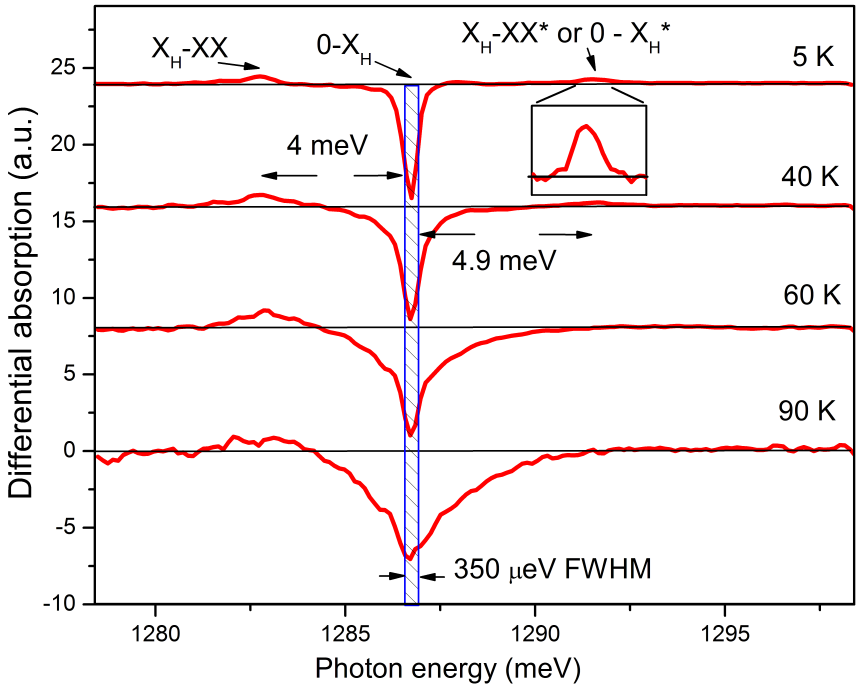

Figure 4.4: Spectral hole burning signals for horizontally polarized pump and probe beams - indicated by the subscripts H. The temperature increases with rows. X denotes an exciton, whereas XX stands for a biexcitonic state. $XX*$ denotes a possible excited biexciton, or $X*$ a charged exciton.

above discussion has proven true, namely the lack of biexcitonic effects.

For low temperatures, and still at $t = 100$ ps, the number of excitons flipping their spin before the probe pulse arrives, can be neglected, thus resulting in the vanishing of the biexciton peak. However, as the temperature is increased, more and more excitons flip their spin within 100 ps, so the probe pulse can therefore create biexcitons. This effect can easily be seen in the graph by following the magnitude of the biexcitonic peak for increasing temperatures.

There have also been results, that have not been initially predicted though. Just like the negative biexcitonic signal, approximately 4 meV below the excitonic peak, a very similar second bump is visible around 4.9 meV above the excitonic peak. One possible explanation for the existence of this signal contribution is the creation of a charged exciton, consisting of an electron-hole pair with an additional charge, either positive through a hole, or negative by an electron. This means that the pump pulse apparently also excites electrons and holes separated one from another, partially trapped in the dots. Since the electric charge changes the dot potential, the original energy structure is lost and, hence, shifted by approximately 5 meV. The signal provides the same sign as a biexciton, since this new compound cannot be formed by the probe in the absence of the pump,

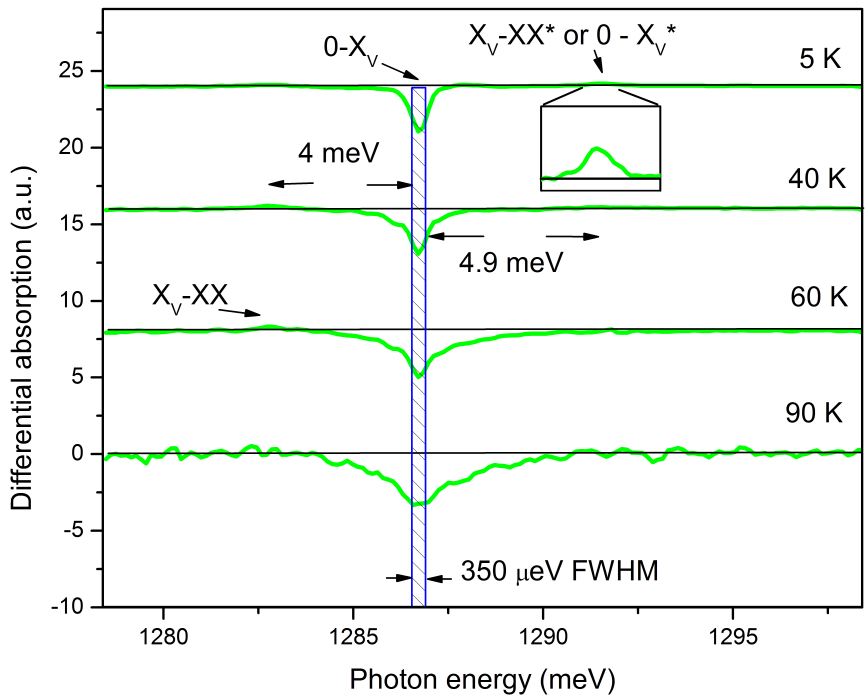

Figure 4.5: Spectral hole burning signals for vertically polarized pump and probe beams - indicated by the subscripts V. The temperature increases with rows. X denotes an exciton, whereas XX stands for a biexcitonic state. $XX*$ denotes a possible excited biexciton, or $X*$ a charged exciton.

analogously to the biexciton.

Another possible explanation of this phenomenon is the state of an excited biexciton. This state can be viewed as the "anti-bonding" state between two excitons, thus with higher binding energy, whereas a ground state biexciton provides its "bonding" counterpart with lower bonding energy [9]. In order to prove this assumption, the pump photon energy must be varied, as well as the temporal evolution has to be measured. Like the "regular" biexciton, the excited biexciton can only be created, if a preexcitation exists, thus an exciton must have the same relaxation time as this excited biexciton.

However, unlike the regular biexciton, as Ikezawa et al. indicate, the excitation photon energy dependence of the distance between the excited biexciton binding energy and the excitation photon energy grows linearly, and having slope 1, with increasing photon energy. Since there have not been any targeted measurements - like distance measurements or temporal decays, to either prove or disprove this aspect in this thesis, it remains speculation. Fig. 4.6 illustrates the polarization dependence at 5 K and provides an overview of the exciton-, biexciton- and the one of unknown origin - state.

A closer look at the graph also reveals a very small bump slightly above the exciton's energy (1). Until now there has been no explanation for this peak. This phenomenon also occurred in every measurement, where the pump bandwidth was small enough not to

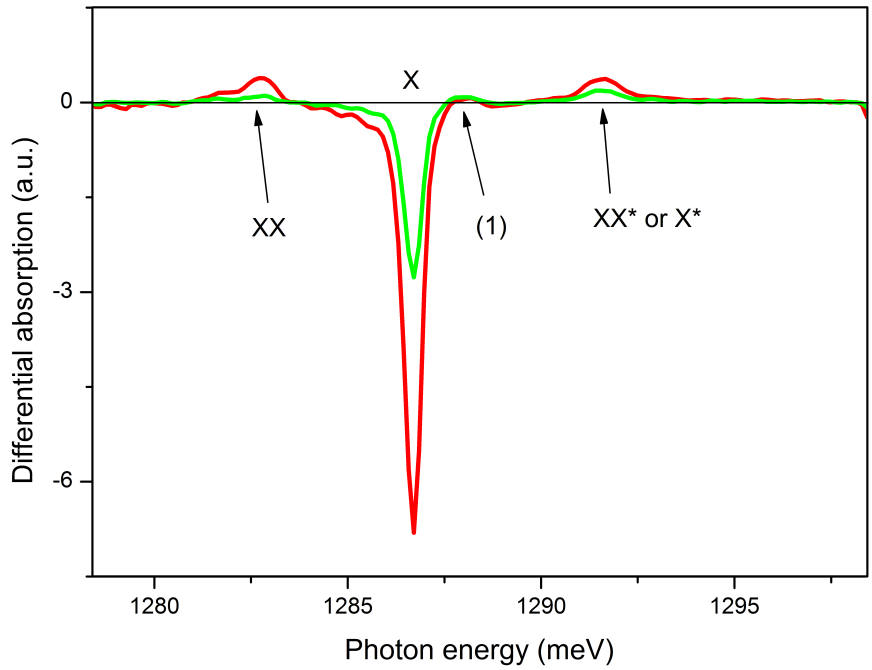

Figure 4.6: Polarization dependence and the consequences: The red line indicates a horizontal polarization of both pump and probe, whereas the green line is due to a vertical polarization of the pump pulse and a horizontal polarization of the probe pulse. Both graphs represent an SHB response at 5 K with a pump FWHM bandwidth of 350 μeV.

cover this peak, and the temperature was low enough, so that it has not been covered by the phonon pedestal either. The signal coverage is a problem in general, when states with a positive contribution are located close to peaks with opposite sign, since the spectral hole burning technique is only able to resolve the total transmission change, and not all the contributions separately.

The spectral hole burning spectra, showing the zero phonon line and the phonon side lobes, as well as the theoretical considerations in the chapter above, distinctly prove a dephasing, that can not be described with a Markovian process, thus a single exponential decay. However, since the spectral hole at 90 K almost looks like a lorentzian line, although it consists of phonon assisted excitonic transitions, and not the excitonic transitions alone, a lorentzian fit to the data has been performed. We will take a full width at half maximum (FWHM) bandwidth criteria as a measure for the frequency corresponding decay time.

A double-sided exponential decaying function is linked to a lorentzian line function via the Fourier transform, hence,

$$f(t) = \frac{1}{\beta} e^{-\frac{\alpha}{\beta}|t|} \Longleftrightarrow F(\omega) = \frac{2\alpha}{\alpha^2 + (\beta\omega)^2}, \tag{4.1}$$

where β is a scaling constant. The alteration of this value will lead to the final FWHM expression. Half of the full width at half maximum in the ω domain, ω_H, is expressed by

$$\frac{1}{2} = \frac{\alpha^2}{\alpha^2 + (\beta\omega_H)^2}. \tag{4.2}$$

This leads to

$$\beta\omega_H = \alpha. \tag{4.3}$$

Since the curve fitting routine used a slightly changed version of the lorentzian function,

$$f(t) = \frac{1}{2}e^{-\frac{\alpha}{2}|t|} \Longleftrightarrow F(\omega) = \frac{2\alpha}{\alpha^2 + (2\omega)^2}, \tag{4.4}$$

where β is simply set 2, this leaves an FWHM criteria of $2\omega_H = \alpha$, where $2\omega_H$ already provides the full width at half maximum bandwidth ω_F, and the decay $\frac{2}{\alpha}$ is simply $\frac{2}{\omega_F}$. Since this decay is assumed to be exponential, it can be interpreted as the dephasing time T_2 of the excitonic state. Hence,

$$T_2 = \frac{2}{\omega_F} \tag{4.5}$$

can be extracted from the data. Fig. 4.7 shows the spectral hole burning data at 90 K, as well as the lorentzian fit. The parameter w, i.e. ω_{FE} in the energy domain in our case,

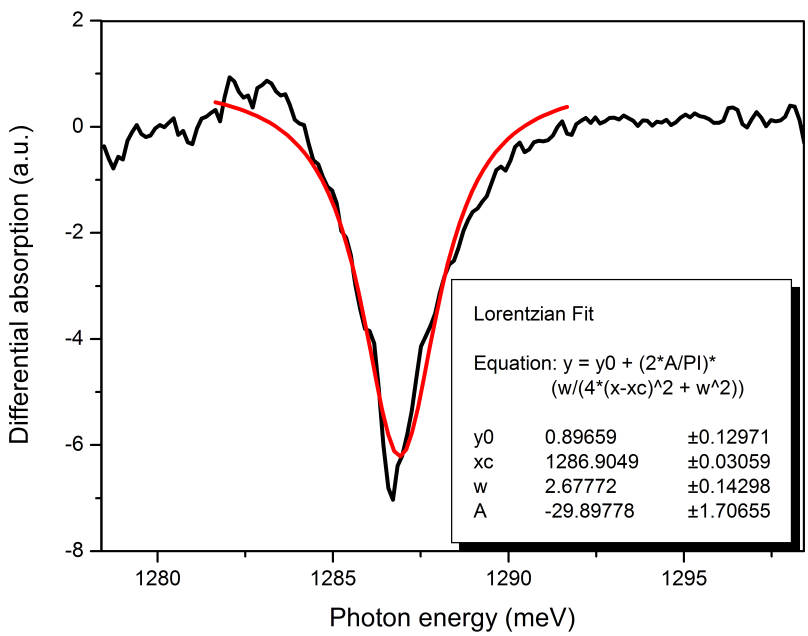

Figure 4.7: Assumption of a single exponential decay as dephasing at high temperatures with the appropriate lorentzian fit

has the value 2.67 meV. This corresponds to an FWHM width in the spectral domain of

$$\omega_F = \frac{\omega_{FE} \cdot q}{\hbar}, \tag{4.6}$$

where ω_{FE} is the FWHM in eV and q denotes the elementary charge of an electron.

T_2 at 90 K is then finally obtained as:

$$T_2 = 0.49ps \tag{4.7}$$

To compare this value to already measured data, fig. 4.8 provides the necessary information needed. An exponential decay with time of the polarization, written as

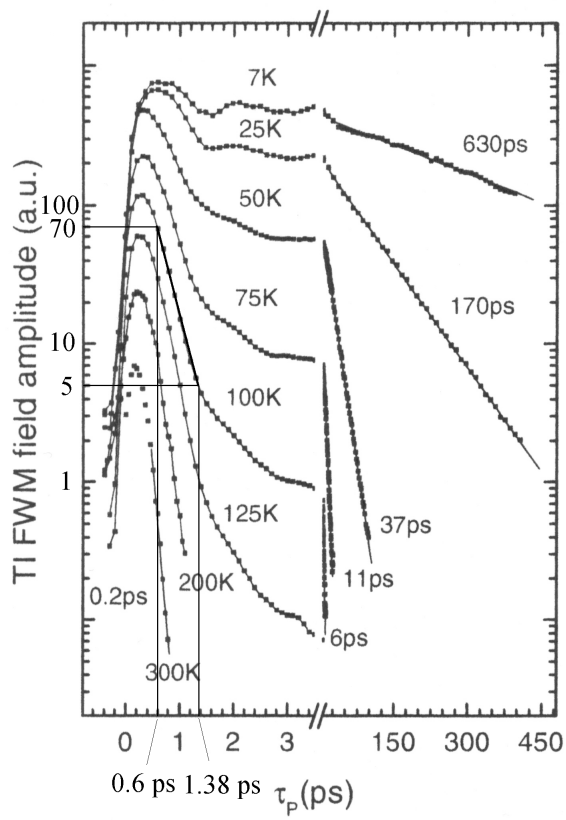

Figure 4.8: Decay of the polarization field amplitude as a direct measure for the loss of phase coherence at different temperatures obtained with a four-wave mixing technique [19]. Phonon induced initial dephasing is also approximated by an exponential decay or, equivalently, by a linear decay in the logarithmic scale as indicated.

$$P(t) = e^{-\frac{2t}{T_2}}, \tag{4.8}$$

becomes in a logarithmic scale using $\log_{10}$

$$\log_{10}[P(t)] = -\frac{2t}{T_2} \cdot \log_{10}(e). \tag{4.9}$$

Fig. 4.8 already provides the scaling factor $\log_{10}(e)$, since the the logarithmic steps are measured in decades. Hence, an exponential decay degenerates to a linear decay on a logarithmic scale.

To apply a fit to the data provided, the line at 100 K has been chosen, since it is the closest temperature to the 90 K of the lorentzian fit in fig. 4.7. One obtains $P_1 = 5$ and $P_2 = 70$, whereas the extracted points from the time axis read as $t_1 = 1.38ps$ and $t_2 = 0.6ps$. The slope of a straight line is simply

$$k = \frac{\Delta y}{\Delta x} = \frac{\log_{10} \frac{P_2}{P_1}}{t_2 - t_1} \equiv -\frac{2 \cdot \log_{10}(e)}{T_2}, \tag{4.10}$$

which eventually leads to

$$T_2 = 0.59ps. \tag{4.11}$$

Since the spectral hole burning response at 90 K seems to be dominated by just the phonon-assisted transitions, a comparison between a lorentzian-like decay of the measurements in this thesis, and the phonon-induced initial fast dephasing - also approximated by a single exponential decay for the sake of comparison, seems very reasonable and leads to very similar results of the dephasing time T_2.

4.3 Measurements with different excitation energies

As already mentioned, the biexciton binding energy does not vary with the exciton energy, leaving the distance between the exciton and the biexciton almost unchanged - at approximately 4 meV. Fig. 4.9 shows three different excitation energies within the inhomogeneous broadening, with all leading to very similar biexcitonic binding energies. These measurements included excitation energies at the center, as well as energies at the edges of the inhomogeneous broadening. To compare the curves in one plot, the spectral detuning between pump and probe has been used instead of the respective absolute excitation energies.

Fig. 4.10 provides some real intriguing aspects of excitation. According to the photoluminescence spectrum of fig. 4.1, an excitation energy of roughly 1330 meV only leaves a small fraction of excitons in the ground state, while an overwhelming majority of the excited states are excited excitons from the p-shell. Since the spectral areas of the shell states overlap - due to the inhomogeneous broadening - there might even be some excitons in the higher d-shell, resulting from 1330 meV pump energy. It should be noted, that the distinct wiggles around $\Delta T \lessgtr 0$ are not induced by noise, but exhibit spectral hole burning data due to excitation. However, the analysis of this data was not part of this thesis.

4.4 Measurements with different excitation bandwidths

In order to observe a clear distinction between the zero-phonon line and the phonon side lobes, all measurements in the previous section have been conducted with a pump pulse bandwidth well below 1 meV FWHM. The results were sharp, and well separated transitions - at least for low temperatures. Fig. 4.11 shows, what happens, if the pump bandwidth is tuned up to 1 meV.

Furthermore, it also indicates an increasingly undeterminable spectral hole burning signal between the excitonic and the biexcitonic transition. Since the bandwidth of both,

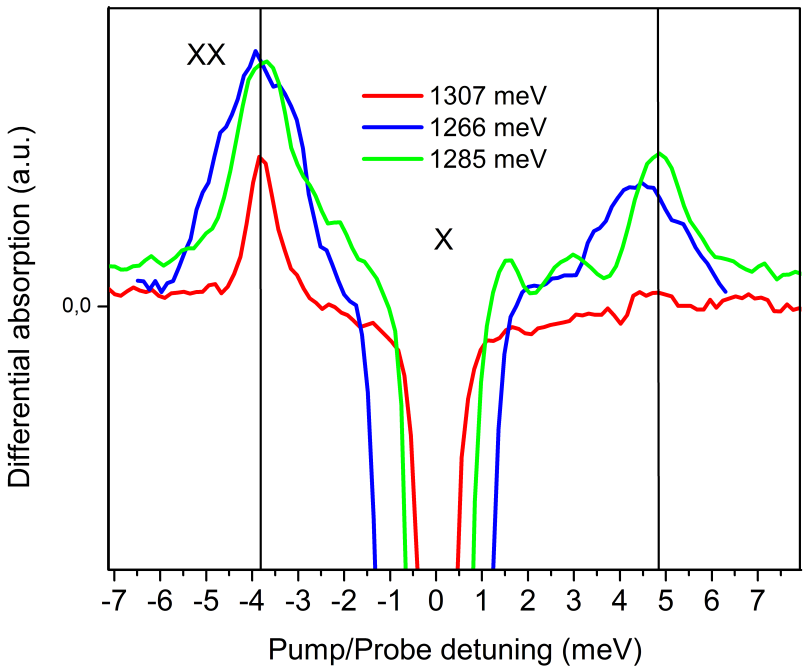

Figure 4.9: Different excitation energies providing almost identical biexciton binding energies of approximately 4 meV. All curves have been measured at 5 K.

the excitons directly excited by the pump pulse and the biexcitons created by pump and probe together, increased, the signals in between of them start to overlap more and more.

The broadest possible spectrum of the pump pulse - only limited by the slit in the pulse shaper - was approximately 3.4 meV. The results of this extremely broad excitation is shown in fig. 4.12. It seems, that contributions of the high energy anti-hole, presumably from a charged exciton or an excited biexciton, getting stronger with increasing excitation bandwidth. Since the distance between the excitonic and the biexcitonic transition is around 4 meV, a pump pulse with spectral components at the biexcitonic transition would create a superposition state of both, an exciton and a biexciton for overlapping energies. Unfortunately, the spectral hole burning signal is not able to resolve this state individually, since the spectral components of the excitonic peak get closer and closer to the ones of the biexcitonic peak. The considerably weaker negative biexcitonic signal contribution gets bleached by the strong spectral hole of the excitonic transition.

Another interesting phenomenon shows up with increasing excitation bandwidth, as indicated by the vertical dashed lines. The whole spectral hole burning response seems to be covered with an additional periodic signal.

Noise as a source of this interference can be excluded, since it appears distinctly periodic with an amplitude proportional to the signal strength - unlike the uncorrelated noise of the whole measurement setup. The periodicity and the signal strength dependence indicate a Fabry - Perot interference, most likely within the sample itself.

To see this, we extract two respective energies from the positions of interference max-

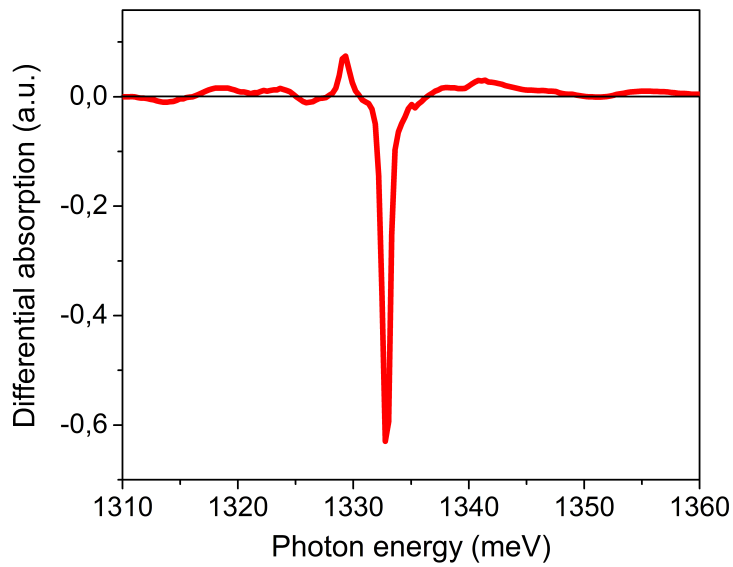

Figure 4.10: Spectral hole burning response of the sample when excited at an energy, where most of the excitonic states occupy the p-shell.

ima. The energies $E_1 = 1285.33055$ meV and $E_2 = 1285.98904$ meV provide a distance of $\Delta E = 658\mu$ eV, corresponding to $\Delta\omega = 10^{12}$ s^{-1}. The Fabry - Perot expression reads as [26]

$$\Delta\omega = \frac{c_0 \pi}{nd \cos\Theta}, \tag{4.12}$$

where c_0 denotes the speed of light in vacuum, n is the refractive index and d the thickness of the sample, and Θ is defined as the angle between a line perpendicular to the surface of the sample and the beam path. Since the sample mainly consists of GaAs, the overall refractive index at the photon anergy of approximately 1285 meV is about 3.5. Since we know the thickness of the sample to be approximately 0.4 mm, we can use the information from above to calculate the corresponding thickness and compare it to the actual one. If we solve for d and setting Θ preliminary to 0 - to get a rough estimate, we will get

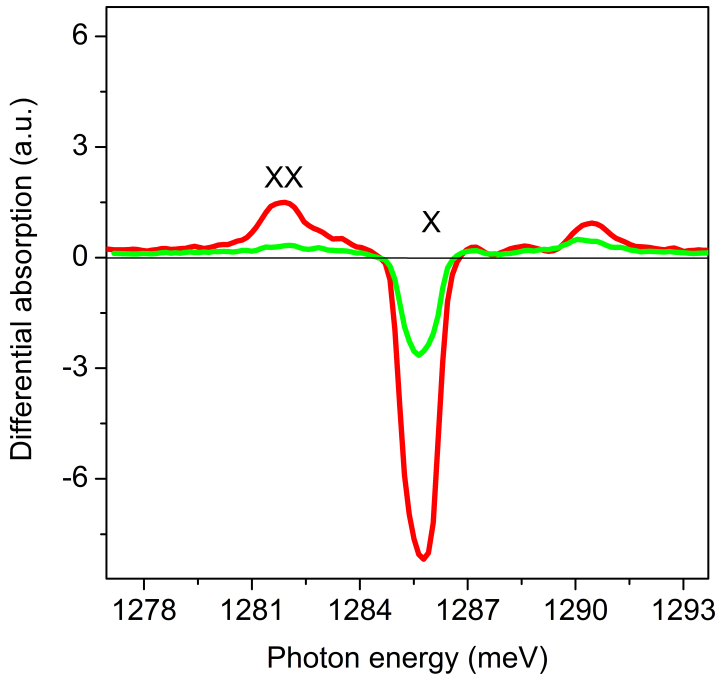

Figure 4.11: Spectral hole burning response with a 1 meV FWHM excitation pulse at 5 K.

$$d = \frac{c_0 \pi}{n \Delta\omega} = 0.27mm. \tag{4.13}$$

This value is very close to the actual thickness of the sample, considering an angle Θ diverging from 0, thus leading to a bigger value of d and all measurement uncertainties. $\Theta \neq 0$ is very likely, since the sample has been placed in the cryostat purposely at an angle in order to just prevent these effects.

This is the reason, why a quarter wave anti-reflection coating for both sides has been added to the sample for further measurements. The thickness of the coating - fourth of the wavelength - refers to a material with a refractive index as the geometric mean of the indices defined by the two adjacent materials constituting a reflectivity. These materials are: Vacuum (within the cryostat) with a refractive index of $n_0 = 1$ and the quantum dot sample, mostly consisting of GaAs with a refractive index of $n_{GaAs} = 3.5$. This leaves a refractive index for the desired quarter wavelength coating of

$$n_{QW} = \sqrt{n_0 \cdot n_{GaAs}} = 1.87. \tag{4.14}$$

The closest refractive index, that is manufacturable, was SiN (silicon nitride) providing $n_{SiN} = 2.02$. Considering a center wavelength of 965 nm, the actual thickness of the quarter wave coating becomes approximately 120 nm. Unfortunately, since the cryostat needed to be removed for the next set of experiments, the coated sample could not be measured in the exact same setting again.

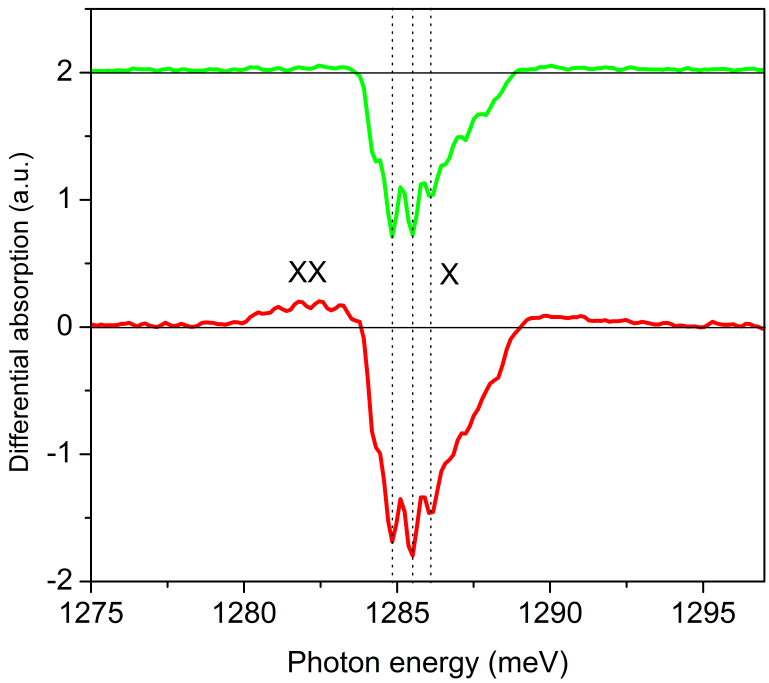

Figure 4.12: Spectral hole burning response with a 3.4 meV FWHM excitation pulse at 5 K. Due to the spectral width and the large magnitude of the excitonic transition, the biexcitonic signal contribution appears weak. The red curve shows data resulting from horizontally polarized pump and probe, whereas the green curve is due to a vertically polarized pump pulse and a horizontally polarized probe pulse.

Chapter 5

Experimental Results - Rabi Oscillations

As already indicated, the threshold in excitation power density, to observe this nonlinear effect in self-assembled InAs/GaAs quantum dots, is in the order of several tens of kW/cm^2 [21]. Chapter 2 already introduced Rabi oscillations as sinusoidal population inversions as a function of the pulse area, for strong optically excited two-level systems. To vary the pulse area, an adjustable attenuator has been used in this thesis.

5.1 Low temperature Rabi oscillations

Before being able to use it, the adjustable attenuator had to be measured itself to serve as a power reference. It consists of a glass plate gradually coated with a metal, to provide a certain spatial attenuation profile (nonlinear). This glass plate was then moved up and down within the pump beam path by a dc motor, to apply the spatial profile as a position/attenuation dependence. The resulting position/signal strength relation, hence, the necessary reference is shown in fig. 5.1.

The next issue was to find the proper shape of the pump pulse. Since an earlier conducted measurement of Rabi oscillations in an inhomogeneously broadened quantum dot ensemble indicated [24], that a sharp rectangular shaped pump spectrum can reduce the influence of the inhomogeneity, as the major contribution to damping, a 3 meV FWHM pulse was used for our measurements. A bandwidth above this value would be prone to simultaneous excitations of excitons and biexcitons, which would definitely contribute to unforeseeable results. Fig. 5.2 shows the corresponding spectrum, that was used for the final Rabi oscillation measurements.

After the pump pulse spectrum has been chosen, its temporal duration is set as well. This leads to the following wavelength and delay time considerations. As it will be shown later, this duration is about 1.5 ps. Furthermore, as it was shown in the previous chapter, the temporal evolution of the excitonic transition around the zero time point was covered with interferences, thus, making the data invaluable. This eventually lead to the choice of the $|X\rangle \longrightarrow |XX\rangle$ probing position. It even turned out, that there were differences in the measurement data depending on the spectral probing position along the biexcitonic transition spectrum. Fig. 5.3 indicates this dependency, by showing four

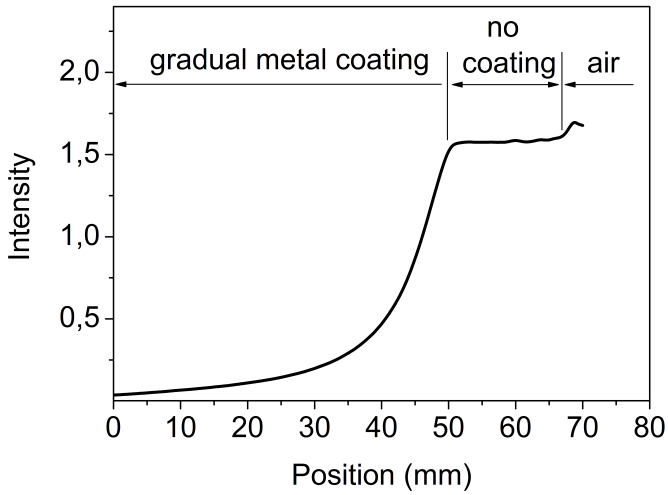

Figure 5.1: Reference curve for the relation between the position of the attenuator and the attenuation/intensity.

different probing positions in the upper graph, and the resulting observations of Rabi oscillations for pulse areas $< 2\pi$ in the lower left graph (original magnitude) and the lower right graph (normalized magnitude). Number (1) is the preferred position (green), since the overall signal appears to be unperturbed by the excitonic contribution, while (2), (3), i.e. the maximum of the biexcitonic signal, and (4) seem to be partially covered by the somewhat stronger excitonic signal with opposite sign. This, of course, changes the overall shape of the curves - as seen in the lower graphs. While (2) and (3) do not indicate a minimum for high power density , (1) already provides a distinct minimum. Due to the energetic proximity of point (4) to the excitonic peak, the low-power signal is even bigger than the high-power signal.

The only downside of this choice is the lower signal strength though, resulting in a bad SNR. This fact can be seen in the lower left graph, where the signal magnitude of (1) is somewhat smaller compared to (2) or (3). The reason for the dependency, as already indicated, arises from the spectral hole burning technique itself. Once two transitions get too close to one another - especially if they provide different signs of their respective contributions - the total change in transmission, i.e. the measurement signal, between them does not reflect their separate contributions.

The observation of the biexcitonic transition does not change the fact, that the actual Rabi oscillations take place between the crystal ground state and the excitonic state, since the excitation is resonant with this transition. Since the biexcitonic signal strength depends on the number of excitons available - which are appearing and vanishing periodically with the Rabi frequency - it is equivalent to the excitonic transition.

Once this particular spectral probing point is established, the temporal evolution of this signal can be tracked over the whole range. As already mentioned, the pump pulse is approximately 1.5 ps long - leading to a temporal probing position for the power intensity dependence of approximately 5 ps.

As it has already been established, the frequency of the periodic population inversion -

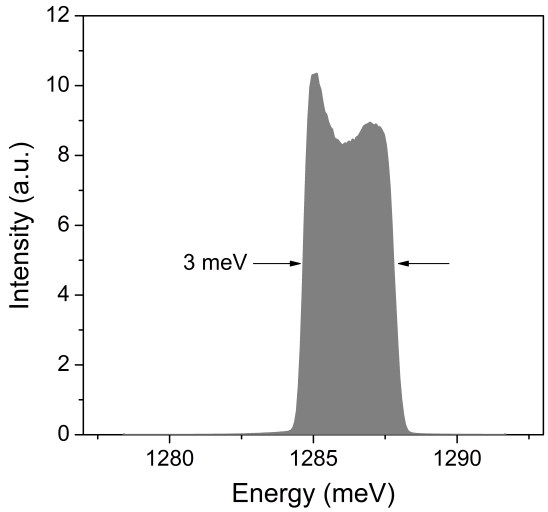

Figure 5.2: Power spectral density versus photon energy of the pump pulse.

the unique Rabi frequency - is proportional to the dipole moment and the strength of the electrical field of the excitation source. Besides the loss of phase coherence of the excitonic state, that leads to a damped oscillation even for single quantum dots, the distribution of the dipole moments - due to the quantum dot size variations - is the most significant contribution to damping in an ensemble of self-assembled quantum dots [24], while the local distribution of the electrical field - approximately Gaussian intensity distribution (due to a Gaussian beam), does not seem to contribute to damping very much at all. So, according to Borri et al., the a priori expectation is to obtain strongly damped Rabi oscillations in the power density region $< 4\pi$.

Since the measurements in this thesis did not consider pulse area variations through a temporal manipulation of the pump pulse, the maximum pulse area is only defined by the amplitude of the pump pulse. This, however, infers that the temporal evolution of the differential transmission signal has to be a damped sinusoid as well, since the short probe pulse samples the longer pump pulse, and therefore observes the change in transmission induced by the pump pulse at the temporal position of the probe, thus, implying a certain pulse area at a certain time.

However, a look at the left four graphs of fig. 5.4 reveals a significant discrepancy from this expectation. Instead of damped sinusoidal oscillations, observed as the pump pulse endures, a Gaussian-like signal seems to surpass everything else during its existence, while its magnitude depends on the pump intensity. The very right graph of fig. 5.4 does indeed show a damped oscillation, which is the Rabi oscillation - a function of the pulse area and, hence, the intensity.

Since this finding is the most important part of this thesis, the Rabi oscillation itself is shown again - separately, in fig. 5.5 as a function of the pulse area. Using the classical view of light - as an electromagnetic wave - the power density in free space, thus the Poynting flux, is given by

$$I = \frac{E^2}{\eta}, \tag{5.1}$$

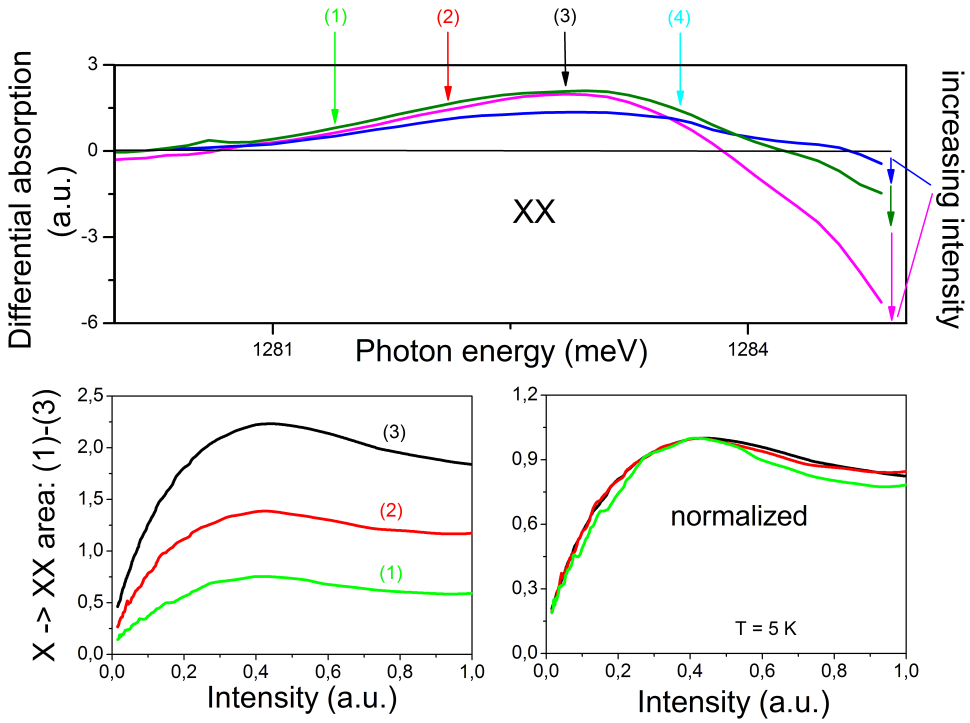

Figure 5.3: Different probing positions (1) - (4) in the adjacency of the biexcitonic transition for different excitation power densities in the upper graph, and probing position-dependent Rabi oscillations with pulse area $< 2\pi$ in the original scale (lower left) and normalized (lower right). Position (1) is optimal, thus, it was chosen for all measurements.

where E denotes the amplitude of the electric field and η is the "wave impedance" of free space, defined as

$$\eta = \sqrt{\frac{\mu_0}{\epsilon_0}}. \tag{5.2}$$

ϵ_0 and μ_0 are the respective free space permittivity and permeability.

Hence, the strength of the electric field is proportional to the square root of the intensity

$$E \sim \sqrt{I}, \tag{5.3}$$

and the pulse area is defined as

$$\Theta = \frac{d_{10}}{\hbar} \int_{-\infty}^{\infty} E(t)\, dt, \tag{5.4}$$

as it has already been depicted in a previous chapter. Again, d_{10} denotes the dipole moment an electrically charged particle, consuming the two possible states $|1\rangle$ and $|0\rangle$, provides, while interacting with the light field, described by the temporal evolution of the amplitude of the electrical field $E(t)$. As already mentioned, pulse area variations in the sets of experiments conducted in this thesis are only based on different attenuations of

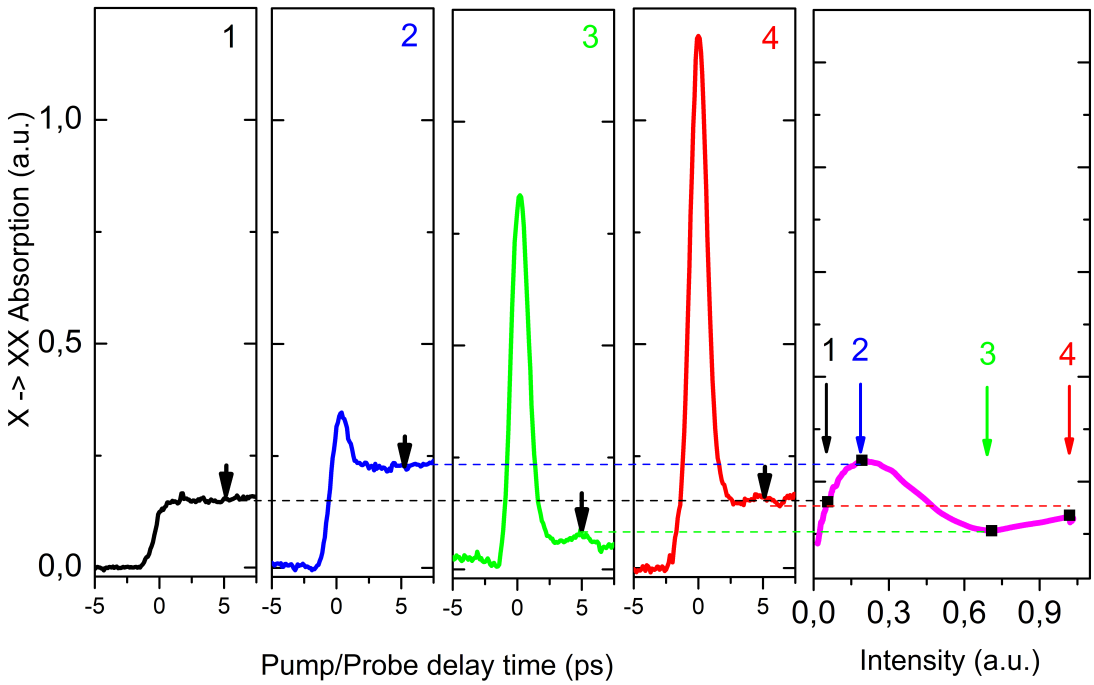

Figure 5.4: Rabi oscillations in an inhomogeneously broadened ensemble of self assembled InAs/GaAs quantum dots at 5 K (I): Temporal evolution of the SHB-signal for increasing excitation power density (left four graphs 1-4, from left to right) and finally the Rabi oscillation itself, although as a function of the intensity instead of the pulse area (right graph).

the pump pulse, and not its temporal duration, which leaves a total dependency of the Pulse area as

$$\Theta \sim \sqrt{I}, \tag{5.5}$$

where I denotes the intensity. This relation is also indicated in fig. 5.5. Unfortunately, as the damping also introduces a shift to the maxima and minima of the oscillation, an uncertainty in the scale of the x-axis is left. The shape in general however, does look very similar to the oscillations found by Borri et al., which indicates the accuracy of these findings.

A possible explanation for the Gaussian-like peak in the temporal evolution of the spectral hole burning signal is a two-photon absorption process. In order to quantify this assumption, the maxima of the peaks are plotted against their respective pump power density, as shown in fig. 5.6 , revealing a somewhat remarkable dependency: The magnitude at the maximum of these peaks seems to be directly proportional to the pump intensity. This infers, that the change in transmission due to this unknown origin grows linearly with the pump intensity. It should be noted, that the excitation density is very high - in order to observe the nonlinear effect of Rabi oscillations, which gives rise to the assumption, that other nonlinear effects can be observed as well.

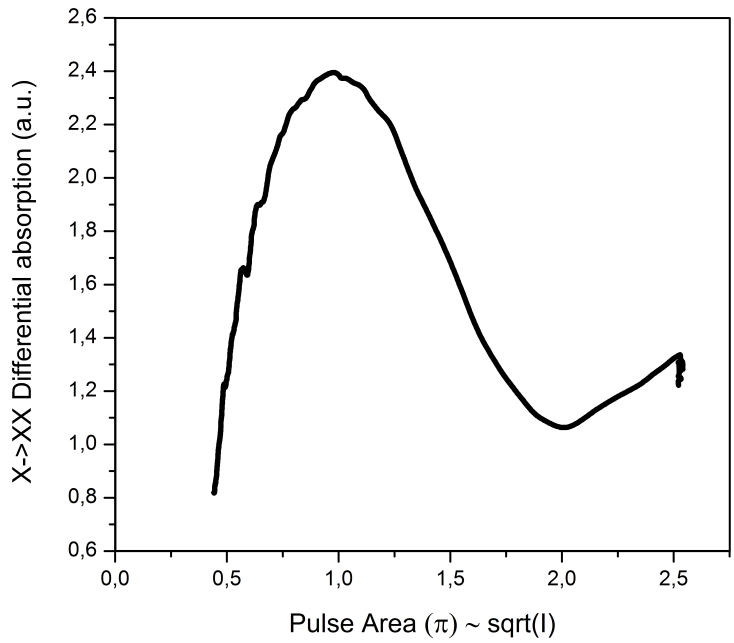

Figure 5.5: Rabi oscillations in an inhomogeneously broadened ensemble of self assembled InAs/GaAs quantum dots at 5 K (II): The classic observation of a Rabi oscillation - Damped sinusoidal population inversion as a function of the pulse area.

The number of photons absorbed in a two-photon absorption process is known to grow quadratically with the power of the photon source [27], hence,

$$n_{TPA} = c \cdot P^2, \tag{5.6}$$

where n_{TPA} denotes the number of photons absorbed by a two-photon absorption process, c is simply a scaling constant, and P is the power of the photon source. Fig. 5.7 shows how absorption can take place in a bulk system having an energy gap higher than the energy of the single photons provided by the probe and the pump pulse. Since the excitation power is extremely high, almost all possible excitonic states are filled, leaving the quantum dot sample almost transparent for both residual pulses, the pump and the probe. Since the sample substrate is made of GaAs, which has a known gap energy of approximately 1.51 eV [26] at low temperatures, it should not absorb either the pump pulse or the probe pulse initially, because their spectral power distribution is centered around 1.285 eV, or, equivalently at 965 nm, and is bound within a range of only 15 meV.

Two-photon absorption however, could lead to an absorption within the substrate. As fig. 5.7 indicates, the strong pump pulse enables a certain amount of carriers interacting with the photons via two-photon absorption. Since the system obviously does not distinguish between photons provided by pump or probe, there is no favor of one type over the other one for taking part in the two-photon absorption process. Only the number of photons getting absorbed depends on the power of the respective contributions, as it can be seen in the different summands of equation (5.7). It has already been mentioned,

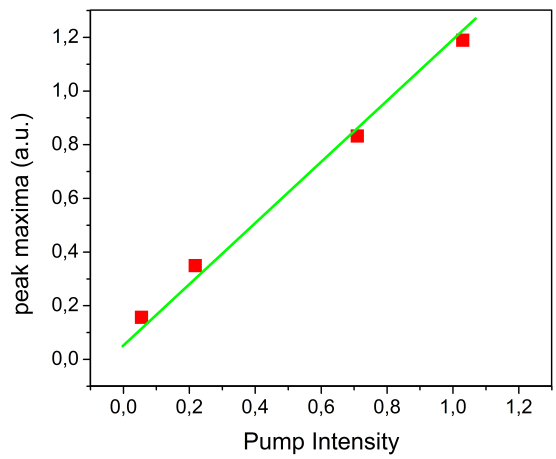

Figure 5.6: Magnitudes of the maxima in the temporal evolution of fig. 5.4 as a function of the underlying pump pulse intensity.

that the ratio between pump and probe power - without attenuation of the pump, was determined as $\frac{P_{probe}}{P_{pump}} = 4\%$. Keeping in mind that the total field is determined by both contributions, equation (5.6) can then be rewritten as

$$\begin{aligned} n_{TPA} = c \cdot P^2 &= c \cdot (P_{pump} + P_{probe})^2 \\ &= c \cdot (P_{pump}^2 + 2P_{pump}P_{probe} + P_{probe}^2) \\ &= c \cdot P_{pump}^2 + c' \cdot P_{pump}P_{probe} + c \cdot P_{probe}^2, \end{aligned} \tag{5.7}$$

where c' is simply $2c$, indicating the two possibilities for a mixed two-photon absorption - a pump- and probe photon, or a probe- and a pump photon. Furthermore, each summand describes the possible contributions - entirely from the pump, a pump and a probe photon , and entirely from the probe. Due to the power ratio, these contributions have a somewhat different magnitude. The summand, entirely determined by the pump pulse, dominates the total number of carriers absorbed. However, the measurement setup does not allow this large contribution to be measured, since only the probe pulse is routed into the spectrometer, and it does not allow the smallest contribution (the one only determined by probe two-photon absorption) to be measured either, since the lock-in technique prohibits signal components apart from the modulation frequency, and only the pump pulse is modulated.

Furthermore, as the change in transmission (absorption) of the pump/probe signal is proportional to the number of absorbed photons of the probe, induced by the pump, this leaves only one possible summand to be displayed:

$$\Delta T = C \cdot P_{pump}P_{probe} \tag{5.8}$$

C denotes the new system constant including the measurement setup and, eventually, since the power of the probe pulse was kept constant over the measurements, the pump/probe signal is then found to be

$$\Delta T = C' \cdot P_{pump}, \tag{5.9}$$

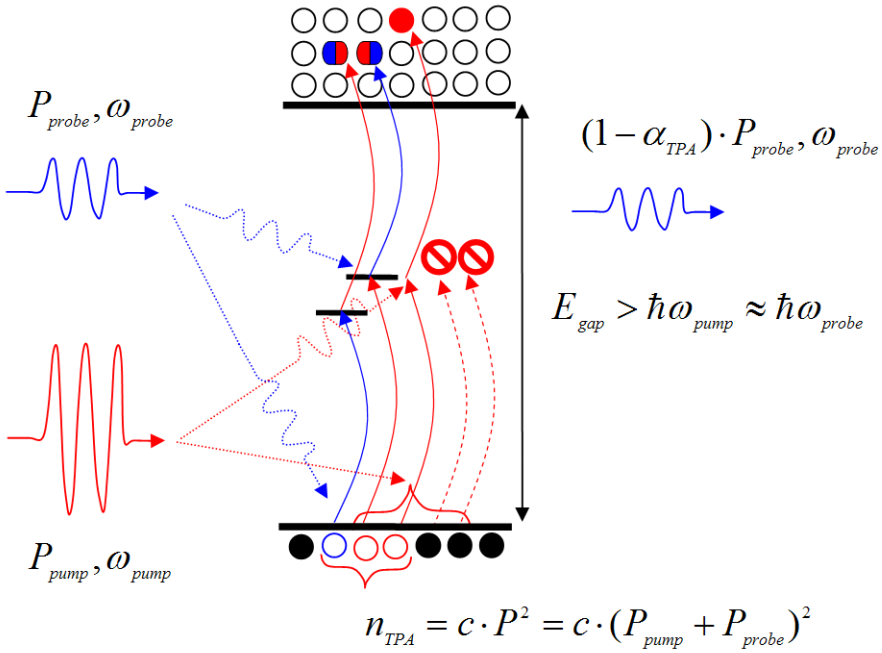

Figure 5.7: Two-photon absorption in a bulk semiconductor material with energy gap E_{gap} bigger than the single photon energies produced by the two sources pump and probe, respectively. $(1 - \alpha_{TPA})$ is the transmission through the material, where α_{TPA} denotes the absorption. The number of photons absorbed by two-photon absorption is known to be quadratic in the excitation power.

where C' includes the constant probe power. Hence, it has been shown, that two-photon absorption would result in a linear pump/probe signal dependence on the pump power. It should be noted, that only two-photon absorption is accounted for a change in transmission, thus ignoring the desired excitonic signal contributions. To further prove this assumption measurements on bulk GaAs have been conducted with similar results. Equation (5.8) infers the presence of this signal, only when both pump and probe, are temporally overlapping. Since the duration of the probe pulse was given by the mode-locked laser system with approximately 80 fs pulse duration, this gave rise to a very convenient way to measure the duration of the pump pulse, eventually leading to the value 1.5 ps and the 5 ps probing position mentioned earlier.

5.2 Temperature dependence of the Rabi oscillations

Besides the impact of inhomogeneous broadening on damping, the dephasing time plays the major role in the observation of a coherent effect. The increasing linewidth, with growing temperature, suggests a very strong temperature dependence of the phase coherence. As all previous measurements in this chapter have been conducted at liquid Helium temperature, fig 5.8 shows the influence of different temperatures on the Rabi oscillations with same maximum pulse area. At 5 K temperature the inhomogeneous broadening effects dominate the contribution to damping - a measure for the dephasing.

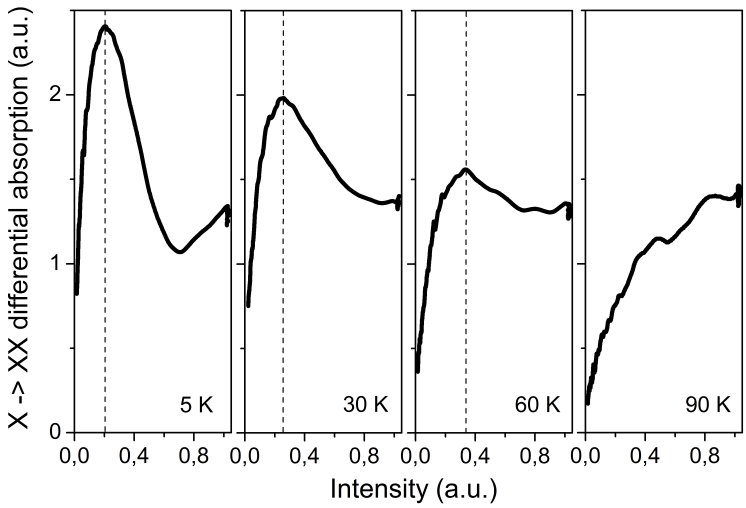

Figure 5.8: Temperature dependence of the Rabi oscillations for equal pulse area/intensity range. As the temperature increases, the phase of the excitonic wave function decays faster, eventually leading to an almost total loss of phase coherence during the excitation for 90 K, manifested in a saturation-like power dependence, with definitely no coherent character.

As the temperature is increased, dephasing of the excitonic state itself surpasses the other contributions. If the dephasing time is smaller than the duration of the pump pulse, the gradual sampling by the probe pulse degenerates to a simple continuous wave power measurement with saturation effects. The measured dephasing time at 90 K of approximately 0.5 ps from above indicates a total loss of phase coherence within the 1.5 ps pump pulse duration.

The dashed vertical lines in 5.8 indicate a shift of the maximum with increasing temperature. It seems, that the original scaling of the pulse area axis is not applicable any more. This effect can be observed, if the pump duration is in the order of the dephasing time of the system [28]. This, of course, is equivalent to the different dephasing times due to temperature variations and a constant pulse duration, as it was the case for measurements in this thesis. Förstner et al. present dephasing mechanisms during nonlinear optical excitation including electron-acoustic phonon interactions - unlike previous considerations of a linear optical regime evaluated within the independent Boson model - which lead to the observation of strongly damped, but still noticeable, Rabi oscillations, even for pulses longer than the dephasing time.

There are two different explanations for the deviation of the measurement results from the theoretical predictions: Firstly, Förstner et al. used GaAs as a model system for the quantum dots, whereas the sample used in this thesis contains InAs quantum dots. And, secondly, the calculation only included homogeneous polarization contributions, thus, ignoring possible inhomogeneous damping contributions to the polarization.

Conclusions and Outlook

In this diploma thesis an inhomogeneously broadened ensemble of quantum dots was investigated using ultrafast spectral hole burning spectroscopy.

The first part of the investigation focused on the temperature-dependence and excitation polarization dependence within the linear excitation regime, while the second part emphasized the effects of strong coherent excitation, eventually leading to Rabi oscillations.

The pump/probe spectra at low temperatures revealed the superposition of the zero phonon lines (ZPL), energetically selected by the pump pulse bandwidth, ranging from 350 μeV to 4 meV. The creation of a biexciton depends on the polarization of the pump and probe pulses. If both have the same polarization, a biexciton is able to be created out of these two contributions. Once the polarization of the pump pulse and the probe pulse are orthogonal, a biexciton cannot be initially created. So the consequences of this fact have been seen in the experiments. If the temperature is low, the spin lifetime of the excitonic state is comparably long, leading to almost no spin flips of the exciton's spin, enabling a maximum number of created biexcitons for equal polarization and zero created biexcitons, if the polarization of pump and probe are orthogonal. Once the temperature increases, more excitons flip their spin leading to an increasing amount of biexcitons for the orthogonally polarized pump/probe case. This effect can be seen for any excitation bandwidth.

If the excitation bandwidth is narrow enough, distinctly separable ZPL and phonon sideband contributions can be observed. As a consequence of the interaction of a localized quantum dot, having certain dimensions, with the acoustic phonon modes, the energetic range of phonons suitable for an interaction is limited. Hence, a limited interval around the excitonic transition is revealed, instead of a steadily with temperature increasing phonon sideband. As already indicated, the sidebands are due to exciton - acoustic phonon interactions, while optical phonon interactions cannot be resolved within the energetic probe window.

A very intriguing aspect of the experiments had to be left behind due to time limitations: Chapter 4 provides only a very brief insight on the spectral hole burning data for an excitation energy centered around the energy of the p-shell. As the data indicates, many processes seem to be involved to produce such a complex spectrum.

Yet another aspect could not be revealed - the energy splitting between horizontally polarized excitons and vertically polarized excitons. In order to resolve this result of anisotropic growth manifestation, the excitation bandwidth has to be kept in the order of some tens of μeV. In order to decrease it, the pulse shaper must be modified. Simply narrowing down the width of the slit does not work on slit dimensions close to the diffraction

limit. So the only way to increase spectral resolution, is by choosing bigger focal lengths of the lenses, thus, expanding the whole pulse shaper setup.

The most remarkable result was the observation of Rabi oscillations. This fundamental effect enables the implementation of a quantum computer, and has been demonstrated in an ensemble of quantum dots only once before. Without damping a pulse with a certain duration and strength, and hence, with a certain pulse area, will cause the system to flip the population between the two levels periodically. The implementation of this population inversion results in the ability to invert a signal, thus, constructing an inverter, eventually leading to a system on which algorithms can be executed - the quantum computer.

Unfortunately, the assumption of an ideal system without damping is not applicable. Finite lifetimes and dephasing mechanisms force the system to loose track of the coherence between the excitation and the polarization, sorely needed for the periodicity. Dephasing is mainly due to the destructive contributions of phonon assisted transitions to the total polarization. The damping results in the need for error correcting codes for quantum computing.

The inhomogeneous broadening worsens the damping scenario, since the different contributions, within the excitation bandwidth range, do not contribute coherently to the polarization, thus, introducing additional damping.

The temperature dependence of the dephasing time becomes manifest in the total vanishing of the Rabi oscillations for higher temperatures. This fundamental aspect has been introduced theoretically, and the measurement results in this thesis are in excellent agreement with these predictions.

Acknowledgements

There are countless people I would like to thank for their constructive contributions to my work. First I would like to thank Prof. Karl Unterrainer for his continuous support in every manner throughout the work on this thesis.

A very special thanks is dedicated to my supervisor Thomas Müller, without whom many of these remarkable results would not have been possible, as well as for his patience for countless hours of fruitful discussions, helping me gaining insight into this sophisticated matter - even during the night.

I would also like to thank Wolfgang Parz for his very helpful advices and discussions during this thesis. I further thank Frederik Schrey for providing a very expensive, yet fragile, cryostat during the whole time needed.

On a personal note I have to thank my parents, who always supported and encouraged me throughout the entire time of my studies at university.

Bibliography

[1] Xiaoqin Li, Duncan Steel, Daniel Gammon and Lu J. Sham:
Quantum Information Processing Based on Optically Driven Semiconductor Quantum Dots
Optics & Photonics News, Volume **38**, September 2004

[2] Peter W. Shor:
Polynomial-Time Algorithms for Prime Factorization and Discrete Logarithms on a Quantum Computer
SIREV Volume **41** Issue 2, Pages 303-332, © 1999 Society for Industrial and Applied Mathematics

[3] Lov K. Grover:
Fixed-Point Quantum Search
Phys. Rev. Lett. Volume **95**, 150501 (2005)

[4] Elisabeth Magerl:
Optical Spectroscopy of Single Self-Assembled Indium-Arsenide/Gallium Arsenide Quantum Dots
Diplomarbeit, Technische Universität Wien (2006)

[5] Daniel Gammon and Duncan G. Steel:
Optical Studies of Single Quantum Dots
Physics Today, Volume **36**, October 2002

[6] A. Zrenner, S. Stufler, P. Ester, and M. Bichler:
Manipulations of a Qubit in a Semiconductor Quantum Dot
Advances in Solid State Physics, Vol. 45, pp. 173-184, ed. by B. Kramer (Vieweg, Braunschweig/Wiesbaden) (2005)

[7] G. Ortner, R. Oulton, H. Kurtze, M. Schwab, D. R. Yakovlev et al.:
Energy Relaxation of Electrons in InAs/GaAs Quantum Dot Molecules
Phys. Rev. B, Volume **72**, 165353 (2005)

[8] K.Zhang, J. Falta, Th. Schmidt, Ch. Heyn, G. Materlik and W. Hansen:
Distribution and Shape of Self-Assembled InAs Quantum Dots Grown on GaAs
Pure Appl. Chem., Volume **32**, 1-331 (2000)

[9] Michio Ikezawa, Yasuaki Masumoto, Toshihide Takagahara and Selvakumar V. Nair:
Biexciton and Triexciton States in Quantum Dots in the Weak Confinement Regime
Phys. Rev. Lett., Volume **79**, Issue 18, November 1997

[10] Claude Cohen-Tannoudji, Bernard Diu, Franck Laloë:
Quantum Mechanics
Whiley-Interscience, New York, 1991

[11] Pawel Hawrylak:
Excitonic Artificial Atoms: Engineering Optical Properties of Quantum Dots
Phys. Rev. B, Volume **60**, Issue 8, 5597-5608 (1999)

[12] P. Borri, W. Langbein and U. Woggon:
Exciton Dephasing via Phonon Interactions in InAs Quantum Dots: Dependence on Quantum Confinement
Phys. Rev. B, Volume **71**, 115328 (2005)

[13] J. Urayama, T. B. Norris, J. Singh and P. Bhattacharya:
Observation of Phonon Bottleneck in Quantum Dot Electronic Relaxation
Phys. Rev. Lett., Volume **86**, 4930 (2001)

[14] P. D. Wang and C. M. Sotomayor Torres:
Multiple-Phonon Relaxation in GaAs-AlGaAs Quantum Well Dots
J. Appl. Phys., Volume **74**, 5047 (1993)

[15] V. Preisler, T. Grange, R. Ferreira, L. A. de Vaulchier, Y. Guldner et al.:
Evidence for Excitonic Polarons in InAs/GaAs Quantum Dots
Phys. Rev. B, Volume **73**, 075320 (2006)

[16] L. Besombes and K. Kheng, L. Marsal and H. Mariette:
Acoustic Phonon Broadening Mechanism in Single Quantum Dot Emission
Phys. Rev. B, Volume **63**, 155307 (2001)

[17] Phedon Palinginis and Hailin Wang, Serguei V. Goupalov, D. S. Citrin, M. Dobrowolska and J. K. Furdyna:
Exciton Dephasing in Self-Assembled CdSe Quantum Dots
Phys. Rev. B, Volume **70**, 073302 (2004)

[18] T. Müller, G. Strasser and K. Unterrainer:
Ultrafast Spectral Hole Burning Spectroscopy of Exciton Spin Flip Processes in InAs/GaAs Quantum Dots
Appl. Phys. Lett., Volume **88**, Issue 1 (2006)

[19] P. Borri, W. Langbein, S. Schneider and U. Woggon:
Ultralong Dephasing Time in InGaAs Quantum Dots
Phys. Rev. Lett., Volume **87**, Issue 15, October 2001

[20] G. S. Agarwal:
Vacuum-Field Rabi Oscillations of Atoms in a cavity
J. Opt. Soc. Am. B, Volume **2**, 480 (1985)

[21] H. Kamada, H. Gotoh, J. Temmyo, T. Takagahara and H. Ando:
Exciton Rabi Oscillation in a Single Quantum Dot
Phys. Rev. Lett., Volume **87**, Issue 24, December 2001

[22] A. Muller, Q. Q. Wang, P. Bianucci and C. K. Shih:
Determination of Anisotropic Dipole Moments in Self-Assembled Quantum Dots Using Rabi Oscillations
Appl. Phys. Lett., Volume **88**, Issue 1 (2006)

[23] T. H. Stievater, Xiaoqin Li, D.G. Steel, D. Gammon, D. S. Katzer, D. Park, C. Piermarocchi and L. J. Sham:
Rabi Oscillations of Excitons in Single Quantum Dots
Phys. Rev. Lett., Volume **87**, Issue 13, September 2001

[24] P. Borri, W. Langbein, S. Schneider and U. Woggon:
Rabi Oscillations in the Excitonic Ground-State Transition of InGaAs quantum dots
Phys. Rev. B, Volume **66**, 081306(R) (2002)

[25] A. M. Weiner, J. P. Heritage and E. M. Kirschner:
High-Resolution Femtosecond Pulse Shaping
J. Opt. Soc. Am. B, Volume **5**, Issue 8, August 1988

[26] Georg A. Reider:
Photonik
Springer-Verlag/Wien, ©1997

[27] Barak Dayan, Avi Pe'er, Asher A. Friesem and Yaron Silberberg:
Two Photon Absorption and Coherent Control with Broadband Down-Converted Light
Phys. Rev. Lett., Volume **93**, Issue 2, July 2004

[28] J. Förstner, C. Weber, J. Danckwerts and A. Knorr:
Phonon-Assisted Damping of Rabi Oscillations in Semiconductor Quantum Dots
Phys. Rev. Lett., Volume **91**, Issue 12, September 2003